Climate Response to Atlantic Meridional Energy Transport Variations

Weimin Jiang, Guillaume Gastineau, Francis Codron

Climate Response to Atlantic Meridional Energy Transport Variations

WEIMIN JIANG,[a] GUILLAUME GASTINEAU,[a] AND FRANCIS CODRON[a]

[a] *UMR LOCEAN, Sorbonne Université/CNRS/IRD/MNHN, Paris, France*

(Manuscript received 18 August 2022, in final form 12 April 2023, accepted 13 April 2023)

ABSTRACT: The climate responses to Atlantic meridional overturning circulation (AMOC) fluctuations are investigated in a hierarchy of sensitivity experiments. We modify the baroclinic component of the North Atlantic Ocean currents online in an atmosphere–ocean general circulation model to reproduce typical AMOC multidecadal variability found in a preindustrial control simulation in the same model. An analogous experiment is also conducted using a slab-ocean experiment. The responses to a strong AMOC include a widespread warming in the Northern Hemisphere and a northward shift of the intertropical convergence zone over the Atlantic Ocean. The driving mechanism of climate responses is then investigated with the changes in the energy flows in the ocean and atmosphere. The large-scale atmospheric changes in the tropics are organized by an anomalous cross-equatorial Hadley circulation transporting energy southward and moisture and heat northward. Changes in the Indo-Pacific Ocean circulation and heat transport, driven by the wind stress associated with the abnormal Hadley cell, damp the atmospheric responses. The lack of Indo-Pacific transport and ocean heat storage leads to amplified atmospheric changes in the slab-ocean experiments, which are further amplified by a positive feedback due to the interhemispheric antisymmetric changes in low cloud cover.

KEYWORDS: North Atlantic Ocean; Meridional overturning circulation; Energy budget/balance; Energy transport; Climate variability

1. Introduction

Ocean currents regulate the global climate by transporting energy from low to high latitudes. The Atlantic meridional overturning circulation (AMOC) is of particular importance, as its deep return flow transports relatively cold North Atlantic Deep Water southward to the Southern Ocean. The resulting northward heat transport overwhelms the poleward transport realized by the wind-driven shallow subtropical cell (STC) in the southern tropical Atlantic Ocean (Johns et al. 2011), leading to a northward oriented oceanic meridional energy transport (OMET) in the Atlantic Ocean along the entire latitude range from 30°S to 80°N (Buckley and Marshall 2016; Ganachaud and Wunsch 2003; Klinger and Marotzke 2000; Talley 2003) with a maximum of about 1.1 PW at 20°N (Trenberth et al. 2019).

Although instrumental observations of the AMOC only exist since 2004 with the RAPID-MOCHA array (Cunningham et al. 2007), paleoproxy records (Caesar et al. 2021; Thornalley et al. 2018), and climate modeling studies (Delworth and Zeng 2012; Jungclaus et al. 2005; Jiang et al. 2021) suggest that the AMOC and associated energy transport exhibit large variability on multidecadal to centennial scales. Additionally, the AMOC is projected to slow down significantly by the end of the twenty-first century in response to global warming (Cheng et al. 2013; Jackson et al. 2022), although there is continued debate about the rate and cause of the decline (Weijer et al. 2020). Given the crucial role of the AMOC in ocean heat redistribution and the limited observations available, it is essential to understand the climate response to the AMOC changes using GCMs.

Some studies use statistical relationships between the AMOC and climate indices in multicentennial simulations of climate models using fixed external forcings (e.g., Delworth and Zeng 2012; Mahajan et al. 2011; Muir and Fedorov 2015, 2017). The impacts of a strong AMOC include a warming of the North Atlantic Ocean surface temperatures, with a local maximum in the subpolar gyre [see Zhang et al. (2019) for a review], a northward shift of the intertropical convergence zone (ITCZ) in the Atlantic Ocean (Menary et al. 2012; Vellinga and Wu 2004), Arctic sea ice loss (Day et al. 2012; Delworth and Zeng 2012; Mahajan et al. 2011; Zhang 2015), and possibly an interhemispheric sea surface temperature (SST) seesaw pattern with cooling in the subtropical Southern Ocean together with North Atlantic warming (Muir and Fedorov 2015). However, the statistical analysis does not distinguish causality. Drivers of AMOC variability may be mixed with responses to AMOC changes.

To isolate the responses to AMOC fluctuations, sensitivity experiments are widely used. For instance, atmospheric models using prescribed SST and sea ice anomalies associated with AMOC variability have shown that warm subpolar Atlantic SST anomalies following an intensification of AMOC gave rise to negative North Atlantic Oscillation (NAO)—like sea level pressure (SLP) anomalies in winter, characterized by dipolar SLP anomalies over the Euro-Atlantic sector (Gastineau et al. 2016). Montade et al. (2015) found that the AMOC surface anomalies also led—in a glacial climate—to latitude shifts of southern westerly winds. However, in these atmosphere-only experiments, the prescribed SSTs act as an infinite source or

Denotes content that is immediately available upon publication as open access.

Supplemental information related to this paper is available at the Journals Online website: https://doi.org/10.1175/JCLI-D-22-0608.s1.

Corresponding author: W. Jiang, weimin.jiang@locean.ipsl.fr

DOI: 10.1175/JCLI-D-22-0608.1

sink of heat. Atmospheric models coupled with a slab-ocean model (SOM) have a more realistic representation of air–sea interactions. Such experiments with a prescribed heat flux anomaly to warm the North Atlantic suggested an impact of the North Atlantic warming in the tropics (L'Hévéder et al. 2015; Hsiao et al. 2022). However, these experiments do not include a dynamical ocean and cannot fully estimate the role of oceanic circulation, especially outside the Atlantic basin. The impacts of AMOC are often overestimated in SOM experiments (Zhang 2017; Kang et al. 2019; Green and Marshall 2017; Tomas et al. 2016).

The impacts of AMOC on climate have also been investigated in atmosphere–ocean GCMs (AOGCMs) with "hosing" experiments in which an artificial freshwater flux is applied into the North Atlantic to inhibit deep convection and hence reduce the AMOC strength (e.g., Stouffer et al. 2006; Zhang and Delworth 2005; Rahmstorf et al. 2005; Mignot et al. 2007; Thomas and Fedorov 2019). The ocean in AOGCMs is fully coupled to the atmosphere, which allows for feedbacks. The AMOC impacts found in these experiments are comparable to those in atmosphere-only or SOM experiments. Reduced AMOC leads to a displacement of the ITCZ over the Pacific Ocean, in the same direction as the Atlantic ITCZ (Zhang and Delworth 2005; Vellinga and Wood 2002). In addition, the effects of freshwater (salt) perturbation on the decay (growth) rate of the AMOC are nonlinear (Brunnabend and Dijkstra 2017). The weakening of the AMOC induced is also sensitive to the location of the freshwater forcing (Smith and Gregory 2009) and the freshwater removal implemented to compensate for hosing (Jackson et al. 2017). Care must be taken with these experiments to disentangle the contribution of the dynamical ocean response from the artifacts resulting from the forcing used. Therefore, an alternative method to properly excite the AMOC fluctuations would be highly beneficial.

In this study, we modify the AMOC in an AOGCM by constraining the baroclinic currents in the North Atlantic using the flow-field correction method derived from Drews et al. (2015) and compare the climate responses to the impacts produced in an equivalent simulation using a SOM. The responses are analyzed by investigating the changes in energy transport and energy budget. The paper is organized as follows. Section 2 describes the experimental design for the AOGCM and SOM. The resulting climate responses are explored in section 3. Changes in the meridional energy transports and radiative feedback are studied in section 4. Discussion of the results and conclusions are provided in section 5.

2. Model and experimental setup

a. Coupled model experiments

We use the low-resolution coupled model IPSL-CM6A-LR (Boucher et al. 2020), which participated in the Coupled Model Intercomparison Project phase 6 (CMIP6) experiment. Its atmospheric component is LMDZ6, with a horizontal resolution of 1.26° × 2.5° and with 79 levels and a top level at 1 Pa. LMDZ6 is coupled to the land surface module ORCHIDEE with the same horizontal grid (Cheruy et al. 2020). The oceanic model is NEMO with the eORCA1 grid with a resolution of about 1°, refined to 1/3° in the equatorial and polar regions and 75 levels. The analyses of this study are based on the first 1200 years of a preindustrial control simulation, hereafter referred to as CTL-CM. As noted by Boucher et al. (2020), in IPSL-CM6A-LR, the leading deep formation sites are located in the Nordic seas and the Labrador Sea. The simulated AMOC maximum at 26.5°N is ~12 Sv (1 Sv ≡ 10^6 m^3 s^{-1}) at ~730 m depth, which is weaker and shallower than the observed 16.9 ± 4.6 Sv at 1000 m from the RAPID-MOCHA array (McCarthy et al. 2015).

The AMOC represents the zonally averaged contribution of baroclinic currents in the Atlantic Ocean. Therefore, to constrain it we alter the baroclinic part of the horizontal pressure gradient force in the horizontal momentum equations, as presented in Drews et al. (2015) and Drews and Greatbatch (2016, 2017). The model calculates the in situ pressure by integrating the hydrostatic equation from the sea level to the depth considered. The flow-field correction is realized by replacing the model in situ density ρ_m with a linear combination of ρ_m and an input in situ density ρ_i in the calculation of the horizontal gradient of the hydrostatic pressure using

$$\frac{\partial p}{\partial z} = -g[(1 - \alpha)\rho_m + \alpha\rho_i],$$

where p is the pressure, z is the depth, and g is the gravity; α is a scalar parameter controlling the intensity of modification.

In our experiments, α is set to 0.7, so that the baroclinic flow is estimated at 70% by the input density ρ_i, and the remaining 30% by the model density ρ_m. The input density is calculated online at each point from input temperature and salinity fields, using the seawater equation of state. As this flow-field correction reduces the Rossby wave speeds and damps eddy activity (Drews et al. 2015), we only apply the correction over a reduced domain. First, we avoid constraining the tropical ocean south of 20°N or the marginal seas located north of 60°N (see black contours in Fig. S1 in the online supplemental material). Second, the deep return flow below 1000 m is similarly not constrained and adjusts to the upper ocean changes. Two smooth transition zones are set up at the meridional boundaries between 10° and 20°N, and 60° and 70°N. The ocean density is only replaced in the calculation of the pressure gradient force and is not modified elsewhere in the model. The sensitivity of the flow field correction to the cutoff depth and α value was explored using the monthly climatological annual cycle from CTL-CM as the input density ρ_i. A deeper depth resulted in a large positive bias in the simulated AMOC compared to that found in CLT-CM (Fig. S2), while a higher α value led to a significant drift in the AMOC and SST fields (Figs. S3 and S4; see also Jiang 2022).

To define the input temperature and salinity—and therefore input density—for the weak or strong AMOC simulations, we first regress the annual three-dimensional temperature and salinity fields from CTL-CM on an annual AMOC index called AMOC LFC1 (Fig. S5), which is the standardized first low-frequency component of the overturning streamfunction. AMOC LFC1 is associated with a basinwide AMOC anomaly, showing

dominant centennial to multicentennial variability (see Jiang et al. 2021). Other indices of the AMOC have been found to yield similar results. These regression patterns are then multiplied by 1.5 to amplify the resulting flow anomalies (but remember that only 70% of the flow is constrained), then added to or subtracted from the monthly climatological annual cycle of CTL-CM. The former is used to calculate the input density of strong AMOC simulations, referred to as SG. The latter is used to obtain the input density of weak AMOC runs, called WK. All simulations use preindustrial fixed external forcings. To ensure the robustness of the results, WK and SG have three members each that last for 100 years. The initial states of the three members are sampled in the years 1850, 2000, and 2080 of CTL-CM, which correspond to neutral, strong, and weak AMOC states, respectively (Fig. S5).

The surface temperature and salinity anomalies used, and the resulting density are provided in Figs. S1d–f. As discussed in Jiang et al. (2021), these patterns show a typical North Atlantic warming associated with a more intense AMOC, accompanied by salinification, as found in other models (Msadek and Frankignoul 2009; Meccia et al. 2023).

b. *Slab-ocean model experiments*

To identify the role of the oceanic dynamical changes, the IPSL-CM6A-LR model's atmospheric component is coupled to a mixed layer ocean of a depth of 50 m. However, the model does not incorporate a sea ice module from NEMO and instead employs a simplified interactive thermodynamic sea ice approach (as described in Liu et al. 2021). To account for the influence of the ocean dynamics in CTL-CM, a prescribed annual cycle of additional heat fluxes, referred to as the Q flux, is imposed on the oceanic mixed layer. In the control experiment, called CTL-SOM, this mean Q flux is derived from the monthly climatology of surface fluxes, SST, and sea ice volume from CTL-CM. To reproduce an intensified AMOC in the SOM experiment, the difference in the total surface heat fluxes between the SG and WK runs is imposed in the Atlantic basin between latitudes 35°S and 80°N. As this applied flux is nonzero, with a value of approximately 0.13 W m^{-2} (totaling 1.7 PW), a compensating cooling of −0.63 W m^{-2} is imposed in the Southern Ocean south of 35°S to prevent any drift. This anomalous heat flux is then added to the mean Q flux and applied in the experiment referred to as SG-SOM (as shown in Fig. 1a). The anomalous flux is calculated using only the first SG and WK members, but we verify that using three members instead leads to a similar anomalous flux.

To examine whether the climate variations are sensitive to the spatial structure of the imposed Q flux, an additional experiment called SGS-SOM is conducted. We compute the mean heat flux anomalies in the Atlantic Ocean from SG-SOM for two regions between 35°–80°N and 35°S–35°N. These values are then utilized to construct uniform flux anomalies in these regions, as shown in Fig. 1b (note the different scales in Figs. 1a and 1b). The same uniform cooling is applied south of 35°S.

Figure 1c illustrates the anomalous meridional energy transport in the Atlantic Ocean implied by the imposed Q fluxes in SG-SOM and SGS-SOM experiments, as given by the integrated heat flux from the North Pole. The implied energy transport anomaly (Fig. 1c, red and blue lines) matches the Atlantic OMET anomaly obtained from the flow field simulations (SG minus WK, black line), with approximately 0.07 PW northward at 30°N in both cases. Despite the surface flux anomalies in the Atlantic basin being the same in the AOGCM and SOM simulations, it is demonstrated in the following section that the ocean heat content (OHC) varies in the AOGCM simulations, leading to the Atlantic OMET differing from the meridional transport implied by the heat flux (see the difference between red and black lines). The SOM simulations are conducted using preindustrial fixed external

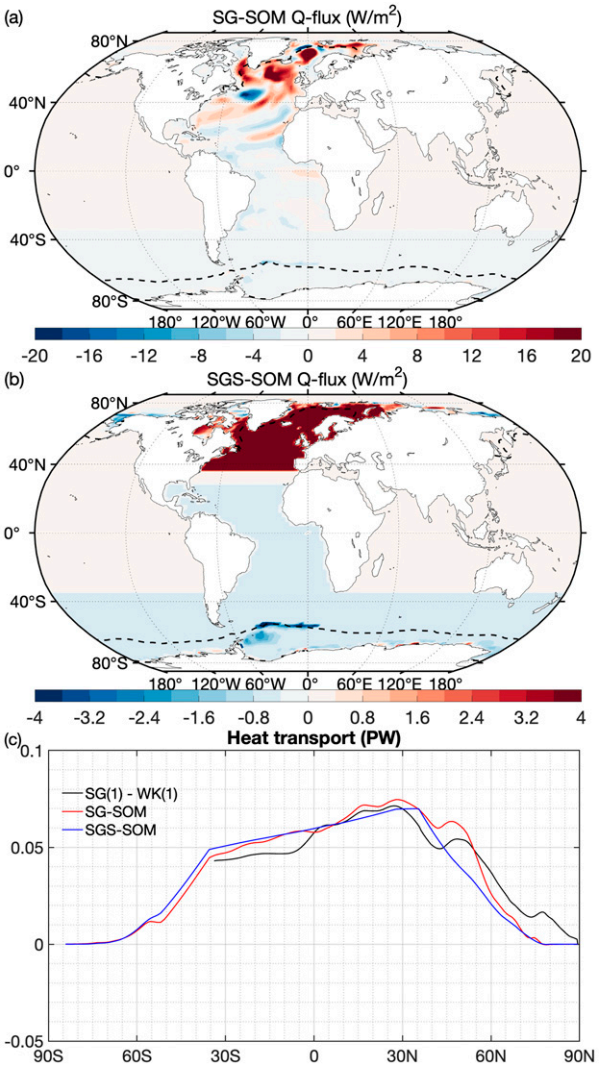

FIG. 1. Anomalous annual mean Q fluxes (W m^{-2}) used in (a) SG-SOM and (b) SGS-SOM. The dashed black lines indicate the 10% level for the annual mean sea ice concentration. Note the different color bars used in (a) and (b). (c) Anomalous ocean meridional energy transport (OMET; PW) implied by the anomalous Q flux in SG-SOM (red) and SGS-SOM (blue). The black line indicates the anomalous Atlantic OMET given by the difference between SG and WK (see text for details).

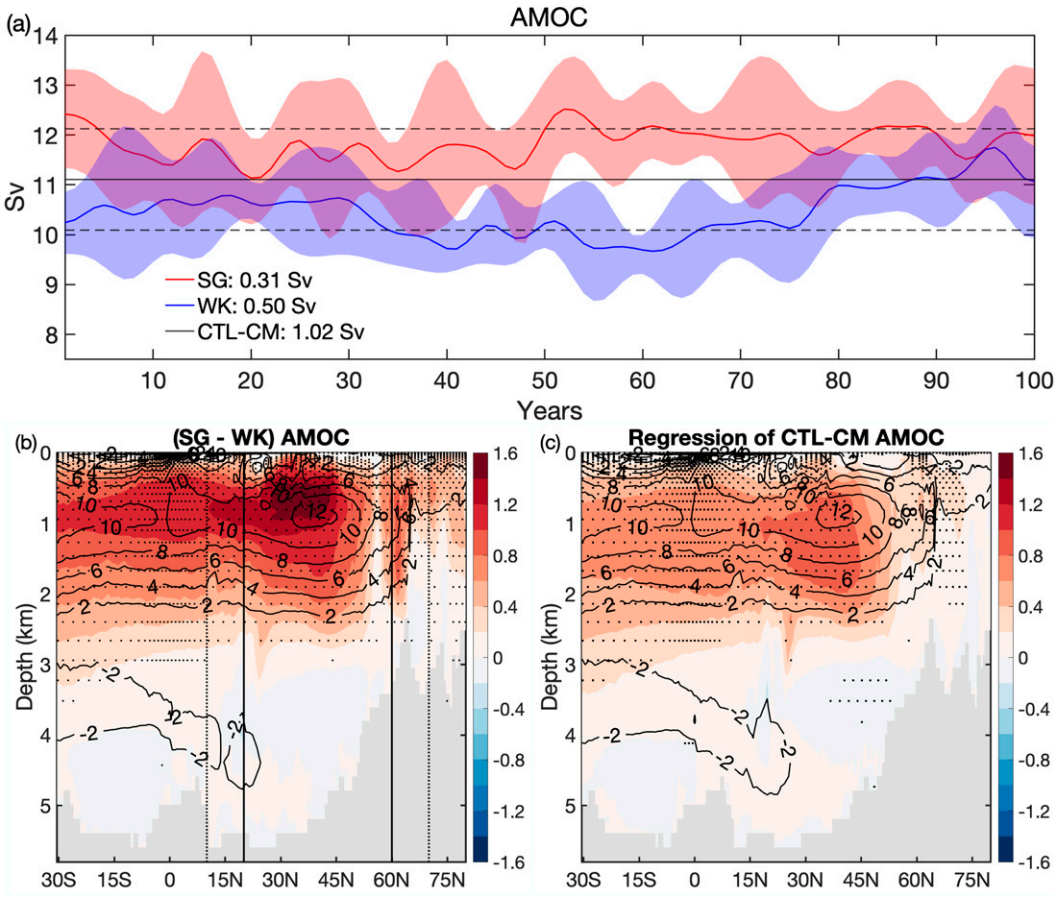

FIG. 2. Comparison of AMOC from the constrained simulations and AMOC from the CTL-CM. (a) Low-pass filtered ensemble mean AMOC at 30°N from SG (red line), WK (blue line), and time averaged AMOC at 30°N in CTL-CM (solid black). Shading indicates the range given by minimum and maximum values of the three members for SG (in red) and WG (in blue) runs. Dashed black lines show the mean ± one standard deviation for CTL-CM. The standard deviations of the low-pass filtered time series are indicated in the panel. (b) Difference (colors) of AMOC between SG and WK and the mean AMOC over all runs (contours). The streamfunction is positive for clockwise rotation. The solid vertical lines indicate the fully constrained area, and dotted vertical lines show the edge of transition zones. (c) Regression of AMOC onto AMOC LFC1 in CTL-CM. The stipples show the 5% significance level.

forcings, utilizing the same initial conditions and lasting for 60 years. The spinup period, consisting of the first 10 years, is discarded.

c. *Statistical methods*

In the following, we illustrate the differences between the ensemble mean of the SG and WK simulations, denoted SG minus WK. The level of significance is established using a two-sample Student t test, assuming equal variance. The e-folding time scale of the AMOC is 20 years in CTL-CM and around 4 years in the flow field corrected AOGCM simulations. To be conservative, all statistical tests for differences are built using the time series from the three members concatenated and averaged by blocks of 20 years. The 20-yr blocks are then assumed to be independent. Changing the size of the blocks to 4 years does not modify the results. Differences between SG and WK using the two halves of the 100 years available (not shown) were calculated and not significantly different compared to using differences over the entire 100 years. Thus, the latter is adopted to increase the number of degrees of freedom.

Meanwhile, the e-folding time scale of surface air temperature is about 2 years in the SOM simulations. Therefore, we use the same method as described above to compute statistical significance in SOM simulations but using blocks of 2 years. The significance for regressions on the AMOC index from the free-running control simulation CTL-CM is calculated using a Monte Carlo method, as discussed in Jiang et al. (2021).

d. *Evaluation of the flow field correction performance*

We compare the AMOC from the coupled simulations with (SG and WK) and without (CTL-CM) flow field correction. Time series of the AMOC strength, defined as the maximum of the meridional streamfunction at 30°N, are plotted in Fig. 2a. A

third-order Butterworth low-pass filter with a cutoff period of 7 years is applied to smooth some of the interannual variability. The AMOC in SG (11.8 Sv) and WK (10.5 Sv) are comparable to the AMOC found in typical strong and weak states in CTL-CM. The standard deviation of the low-pass filtered annual mean AMOC is 0.31 (0.5) in SG (WK), which is smaller than that of CTL-CM (1.02 Sv), likely due to the flow field correction applied toward a fixed AMOC. The mean AMOC remains stable at an intensified or weakened state in the SG and WK ensemble simulations, respectively. However, we notice increases in the AMOC of WK in the last 15 years. Such an increase in WK run is likely related to the salinity-driven multicentennial internal variability of the AMOC found in CTL-CM (Jiang et al. 2021).

The pattern of the Atlantic meridional streamfunction anomaly given by the difference between SG and WK is similar to the analogous regression on AMOC LFC1 in CTL-CM, even in regions outside where the flow is constrained (Figs. 2b,c). Both anomalies maximize between 30° and 45°N. The anomalies in the sensitivity experiments are concentrated at 700 m in SG minus WK and 1300 m in CTL-CM. Besides, the amplitude of anomalies is 1.6 Sv in SG minus WK, larger than the 0.9 Sv maximum in CTL-CM (Figs. 2b,c). However, the anomalies for SG minus WK correspond to that obtained from 1.5 minus −1.5 AMOC standard anomalies. Moreover, the input density only accounts for 70% of the total density when applying the flow field correction (see section 2a). Thus, the amplitude of SG minus WK should be compared to that obtained with two ($1.5 \times 2 \times 0.7 = 2.1$) AMOC standard anomalies. The amplitude of AMOC differences in the constrained simulations (1.6 Sv) is, in fact, slightly smaller than the 2 times the standard AMOC anomaly from CTL-CM ($0.9 \times 2.1 = 1.89$ Sv). Thus, the AMOC anomaly obtained when using the flow field correction is comparable to the one expected from the density anomaly used.

The comparisons of SST, sea surface salinity, and surface density anomalies also indicate a broad agreement between SG minus WK and the analogous regressions on AMOC-LFC1 from CTL-CM (Fig. S1). Within the flow field correction domain, the pattern of density anomaly resembles that of salinity, with positive anomalies in the eastern subtropical gyre and the western subpolar gyre. A local minimum is simulated off Newfoundland, presumably associated with an AMOC-driven shift of the North Atlantic Current (Kwon and Frankignoul 2014; Zhang and Vallis 2007). The main difference is located in the eastern subpolar region, where the flow-field corrected runs show a negative salinity anomaly. In contrast, the regressions from the free run find positive salinity anomalies.

The amplitude of the salinity in SG minus WK is comparable to, or slightly smaller than that obtained through a regression on the AMOC index in the free run. Nevertheless, these anomalies are smaller than those obtained with regressions multiplied by two, showing that flow-field corrected runs produce smaller surface anomalies than the one expected from the density anomaly used. The density anomalies mainly reflect the salinity variations, with wide salinization in the subpolar gyre and eastern subtropical gyre. Outside the domain where the flow field correction is applied, SG minus WK also reproduces the main features of the AMOC regressions, for instance, a negative salinity anomaly in the Arctic. Jiang et al. (2021) suggested that an intensified AMOC is responsible for a slow buildup of Arctic freshwater anomaly in this model, which flushes into the Nordic seas after about six decades, acting as negative feedback on the AMOC strength. Figure S1b, therefore, demonstrates that the reproduced AMOC in sensitivity experiments can generate the Arctic freshwater anomaly. The increase in AMOC strength in the late 15 years of the WK run (Fig. 2a) is consistent with delayed feedback expected from the flush of the Arctic salinity anomalies. This feedback is presumably less active in the constrained runs, as only 30% of the baroclinic current is in balance with the actual model density.

Next, we analyze the climate impacts of the AMOC fluctuations.

3. Climate responses

The difference between SG and WK is investigated to reveal the AMOC climate impacts. The annual mean near-surface air temperature difference between SG and WK (Fig. 3a) shows widespread warming of ~0.8°C in the high-latitude Northern Hemisphere. The warming is maximum over the subpolar Atlantic, Arctic, and North Pacific with an amplitude between 0.25° and 0.5°C. It also extends into the continents, although with a smaller amplitude. The warm anomaly reaches up to 1.5°C in the Labrador Sea and 2.5°C at the Arctic sea ice edge due to the increase in sensible heat from the ocean to the atmosphere associated with Arctic sea ice loss (Mahajan et al. 2011; Moore et al. 2014). Conversely, there is a slight cooling of about 0.1°C above the Southern Hemisphere oceans, visible in the south of the Atlantic, Indian, and Southern Oceans.

The SLP for SG minus WK (Fig. 3c) shows a negative anomaly over Europe, the Mediterranean Sea, and North Africa. Over the North Atlantic region, the geopotential height anomaly (Fig. 3e) is primarily positive north of 40°N, with a maximum over the Nordic seas. This indicates a thermal low structure in the lower troposphere, as typically linked to the warming ocean surface in the North Atlantic (Sutton and Hodson 2005; Hodson et al. 2010). A similar structure more centered over the Arctic also typically appears as a response to sea ice loss (Deser et al. 2015; Screen et al. 2018). Both the SLP and geopotential height anomalies are also positive over the Aleutian Islands, indicating a barotropic atmospheric response. Last, negative SLP is also found in the tropical southern Atlantic and Indian Oceans, associated with the adjustment of the marine atmospheric planetary boundary layer to the cold surface temperature anomalies (Lindzen and Nigam 1987). The anomalies in summer and winter (not shown) resemble the annual mean results.

Compared to AOGCM simulations, the surface warming in SG-SOM minus CT-SOM is more substantial (ranging from 1° to 1.5°C) and more confined to the North Atlantic subpolar gyre, with little impact on the Arctic Ocean (Fig. 3b). This is explained by the use of a 50-m mixed layer depth, which is shallower in the subpolar regions than the actual mixed layer depth in the coupled model. In the SOM simulations, the anomalous Q flux

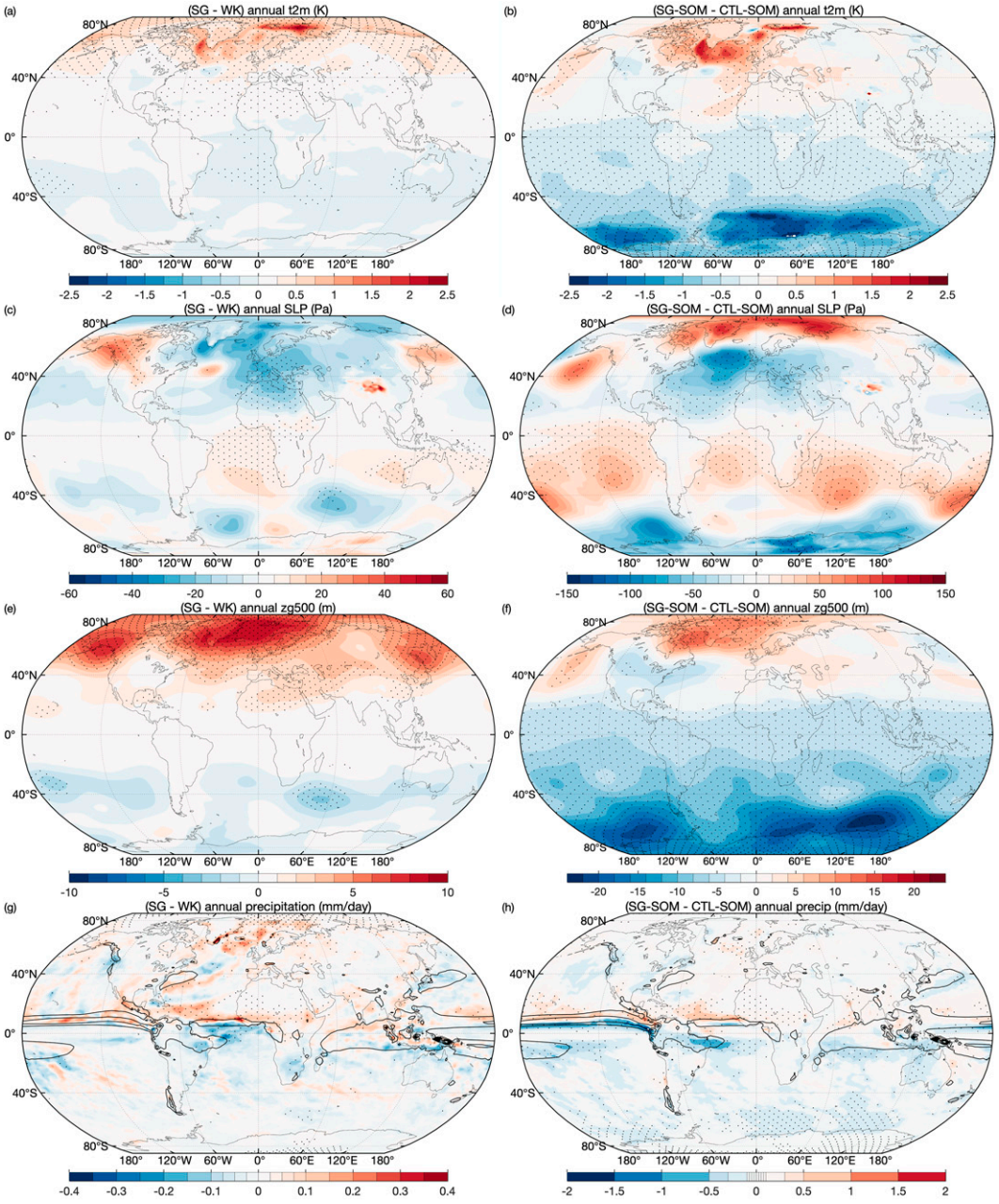

FIG. 3. Annual mean (a) air temperature at 2 m (K), (c) SLP (Pa), (e) geopotential height at 500 hPa (m), and (g) precipitation (mm day^{-1}) for SG minus WK. (b),(d),(f),(h) As in (a), (c), (e), and (g), but for SG-SOM minus CTL-SOM. The black contours in (g) and (h) indicate the mean precipitation (contour interval 5 mm day^{-1}). The stipples indicate the 5% significance level. Note the different scales in the left and right columns.

also ends at 80°N (Figs. 1a,b), meaning that there are no direct AMOC impacts expected north of 80°N. A significant cooling is also simulated in the Southern Hemisphere, with the most extensive cooling occurring between 60° and 80°S. This cooling is interpreted as a consequence of the heat flux applied in the Southern Hemisphere to compensate for the Atlantic warming.

Meanwhile, the SLP (Fig. 3d) of SG-SOM minus CT-SOM shows negative anomalies over the North Atlantic that extend toward Europe and the Mediterranean region. Positive SLP anomalies are also simulated north of the Island so that the dipolar anomalies over the North Atlantic resemble the negative phase of the NAO, as found in previous studies investigating the AMOC or AMV impacts (Gastineau and Frankignoul 2015; Peings and Magnusdottir 2014; Zhang et al. 2019). Nevertheless, the 500-hPa geopotential height anomalies between 10° and 50°N over the North Atlantic are insignificant. The atmospheric

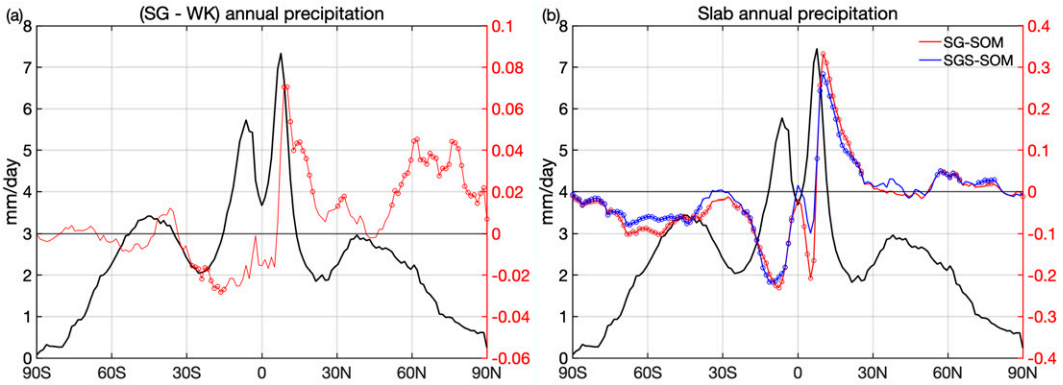

FIG. 4. (a) Climatological (black, left y axis) and anomalous (red, right y axis) zonal mean precipitation (mm day^{-1}) in the AOGCM simulations. (b) As in (a), but for the SG-SOM (red) and SGS-SOM (blue) simulations. Circles denote the significance level below 5%. Note the difference in the right y axis in (a) and (b).

circulation anomalies are baroclinic south of 50°N over the North Atlantic, as in SG minus WK (Fig. 3f). Positive geopotential height anomalies are found over Greenland and the Nordic seas, which is probably linked to the increase of the lower troposphere thickness associated to sea ice loss. Negative 500-hPa geopotential height anomalies are simulated in the Southern Hemisphere, associated with the Southern Hemisphere cooling and associated sea ice growth. Positive SLP anomalies are also simulated in all the Southern Hemisphere tropical oceans, due to surface cooling (Lindzen and Nigam 1987). Last, positive SLP and 500-hPa geopotential height anomalies are found over the Aleutians (Fig. 3f). These barotropic anomalies over the North Pacific also occur in SG minus WK.

In the difference between SG and WK, changes in precipitation are concentrated in the tropical and subpolar Atlantic (Fig. 3g). Over the Atlantic Ocean, rainfall increases north of the equator from the Caribbean Sea to the Sahel and decreases south of the equator from northeastern Brazil to the Gulf of Guinea. This is manifested by a northward shift of the zonal mean precipitation (Fig. 4a). Such northward displacement of ITCZ has long been recognized as linked to the interhemispheric thermal gradients (e.g., Chiang and Friedman 2012; Green and Marshall 2017; Schneider et al. 2014; Sutton and Hodson 2007). The SG minus WK rainfall also increases in the North Atlantic Ocean as the surface air temperature warms. For instance, a significant increase is simulated over the subpolar eastern Atlantic, the Nordic seas, or the Labrador Sea. In the Arctic, SG minus WK also presents a slight increase in precipitation. Last, we note a local increase in rainfall over northwestern India and eastern Asia.

Some of the precipitation changes are reproduced in the SG-SOM minus CT-SOM difference (Figs. 3h and 4b). For instance, the northward ITCZ shift in the Atlantic Ocean is simulated with the same spatial pattern. However, the rainfall changes are larger than in SG minus WK (note the different color scales in Figs. 3g and 3h). The increase of precipitation over the northeastern subpolar Atlantic and northwestern India is also well presented in the SOM simulations. Nevertheless, a northward shift of the ITCZ occurs in the Pacific Ocean, different from SG minus WK changes. A widespread decrease in midlatitude rainfall is shown over the Southern Hemisphere, consistent with the cold anomalies (Figs. 3b).

The zonal-mean precipitation shows an increase of rainfall on the northern edge for the ITCZ at 10°N for SG minus WK (Fig. 4a). An overall rainfall increase is also shown from 55° to 90°N. The SOM simulations show a clear northward shift of the ITCZ, with significant dipolar anomalies at 5° and 10°N, while the ITCZ south of the equator decreases (Fig. 4b). The precipitation changes in SOM are consistent in the tropical Atlantic and Pacific Oceans (Fig. 3h). The increase at 10°N is 0.07 mm day^{-1} in SG minus WK compared to 0.32 mm day^{-1} in the SOM simulations (Fig. 4). The tropical rainfall anomaly is, therefore, 4 times larger in SOM than that in the AOGCM experiments. In the northern midlatitudes, a comparable increase in the precipitation, 0.04 mm day^{-1}, is found in the SOM and AOGCM experiments (Fig. 4). Figure 4 also compares the SG-SOM (red line) to SGS-SOM (blue line). The tropical zonal-mean rainfall shifts and the intensification in northern midlatitudes are similar in the two experiments. Therefore, the spatial pattern of the flux anomaly imposed in the SOM experiments does play an important role.

In summary, SG minus WK shows warming in the North Atlantic extending to the Arctic and Eurasian continent, while in SOM, it is larger and more confined to the Atlantic basin. The atmospheric circulation changes over the North Atlantic–Europe sector are mainly baroclinic and consistent with lower-tropospheric warming with comparable amplitudes. In the tropics, both models simulate a northward shift of the Atlantic ITCZ. But this migration is more pronounced in the SOM and is also simulated in the Pacific Ocean. This suggests that the changes in the ocean circulation outside the Atlantic act to damp the tropical atmospheric response. We next diagnose the meridional atmospheric and oceanic energy transports to better understand these different responses to a stronger AMOC.

4. Analysis of the meridional energy transport

a. Meridional energy budget

The OMET is computed using the sum over the ocean grid of the vertically integrated meridional heat transport, calculated online in the ocean model at each grid point. We also decompose the global OMET into its Atlantic and Indo-Pacific components by only using the grid points in these two oceanic basins. To better understand the redistribution of heat in the ocean, we compute at each latitude a simple energy budget integrated zonally and from the South Pole as follows:

$$\int_{\varphi_s}^{\varphi} \frac{\Delta \mathrm{OHC}}{\Delta t} R_T^2 \cos\varphi' \, d\varphi' + \mathrm{OMET}(\varphi) = \int_{\varphi_s}^{\varphi} \mathrm{HF} \, R_T^2 \cos\varphi' \, d\varphi' + R, \quad (1)$$

where φ' is the latitude used as the variable of integration, φ_s is the latitude of the South Pole, and φ the northern edge of the region of integration; R_T is Earth's radius. The ΔOHC denotes the (zonal-mean) change of OHC during the period Δt, corresponding to the OHC difference between the last and the first time steps. The OHC is calculated as an integral over the depth of the ocean:

$$\mathrm{OHC} = C_{p,w} \int_{-H}^{0} \rho T \, dz, \quad (2)$$

where ρ and T are the density and potential temperature of the seawater, z is the depth, and $C_{p,w}$ is the specific heat capacity of the seawater at constant pressure. HF is the total heat flux entering the ocean (i.e., positive downward); R is a small residue remaining because the integration of the fluxes received by the ocean does not fully account for the OHC variations of the IPSL-CM6-LR (Mignot et al. 2021). Equation (1) thus expresses that the total surface fluxes entering the ocean (first term on the rhs) are balanced either by local heat storage (first term on lhs) or energy transport divergence (second term on lhs). It is expressed as transports: the heat transport implied by the OHC changes (i.e., the transport that would exactly balance the OHC change) plus the actual OMET should equal the transport implied by the surface heat flux.

The total meridional energy transport implied by flux at the top of the atmosphere (TOA) is computed as the meridional integral from the South Pole of the net TOA flux on the atmospheric grid. The net TOA flux in AOGCM is nonzero due to the potential heat storage variation in the ocean and the small nonconservation in the atmosphere (Hobbs et al. 2016; Mignot et al. 2021). To remove the small nonconservation term, the time-averaged global mean TOA flux value is removed from the TOA flux before calculation. The atmospheric meridional energy transport (AMET) is computed similarly but using the difference between the net radiative forcing flux at the TOA and the net air–sea heat flux.

In the AOGCM simulations, the mean OMET dominates in the tropics with an amplitude of 1.5 PW at 15°N/S, while the AMET peaks at 45°N/S with 5–5.5 PW (Fig. S6). The main features are consistent with estimations derived from satellite observations of TOA net forcing, OHC estimations, and atmospheric reanalysis data (Trenberth et al. 2019), except that the OMET is generally underestimated in the IPSL-CM6A-LR model compared to direct observations (Boucher et al. 2020).

In SG minus WK, the stronger AMOC leads to an intensified northward OMET in the two hemispheres, with a maximum of 0.065 PW at 30°N (Fig. 5a, blue line). The energy transport anomaly implied by the TOA radiative flux remains small (Fig. 5a, black line), only showing opposite anomalies between the Southern Hemisphere from 60° to 20°S and tropics from 10°S to 15°N, although the tropical variations are not significant. The AMET and OMET partly balance one another, consistent with the phenomenon known as the Bjerknes compensation (Bjerknes 1964). Indeed, the AMET (Fig. 5a, red line) anomaly is almost symmetrically opposite to the anomalous OMET. However, their sum differs from zero. The amplitude of OMET exceeds that of AMET by about −0.02 PW (or 30% of OMET) at 30°N. This discrepancy is due to the storage of heat in the ocean. SG minus WK shows a decrease of 49 ZJ (1 ZJ = 10^{21} J) of the global OHC. A large part of the OHC decrease occurs in the Southern Ocean. However, a reduction is also located outside the Southern Ocean, for instance, in the Indian and North Pacific (not shown). The transport implied by the OHC change (Fig. 5b, brown line) is oriented southward and is not zero at 90°N. The OMET is partly compensated by heat storage. Surface fluxes (Fig. 5b, green line) only balance about half of the northward OMET on average. The residual is minor and negligible (Fig. 5b, dashed line).

The northward OMET anomaly in the Atlantic Ocean (Fig. 5c, brown line) in SG minus WK is also partially balanced by a southward transport in the Indo-Pacific (Fig. 5c, green line), further reducing the total OMET. The northward anomalous Atlantic OMET is positive and peaks at 0.07 PW at 30°N, while the anomaly in the Indo-Pacific has an opposite sign and shows a minimum of −0.03 PW at 5°S–5°N. The Indo-Pacific component of the OMET has about the same amplitude and sign as the southward AMET at the equator (cf. Fig. 5a and Fig. 5c).

The heat transport implied by the anomalous Q flux in the difference between SG-SOM and CT-SOM is almost equal to the Atlantic OMET in SG minus WK (brown lines in Figs. 5c,d). The slight difference is accounted for by the heat storage changes (see section 2b). Nevertheless, the amplitude of the southward AMET anomaly (Fig. 5d, red line) reaches twice the implied OMET at the equator or almost 4 times that of the AMET anomaly in SG minus WK (see the different y axes for Figs. 5a and 5d). This increased AMET is consistent with the energy transport implied by the net TOA radiative flux, which shows a large southward component between 30°S and 30°N, peaking at −0.08 PW at 8°N.

b. Large-scale circulation changes

We calculate the atmospheric zonal mean meridional overturning circulation to investigate the Hadley circulation (Fig. 6), which is closely related to the AMET in the tropics. Both the AOGCM

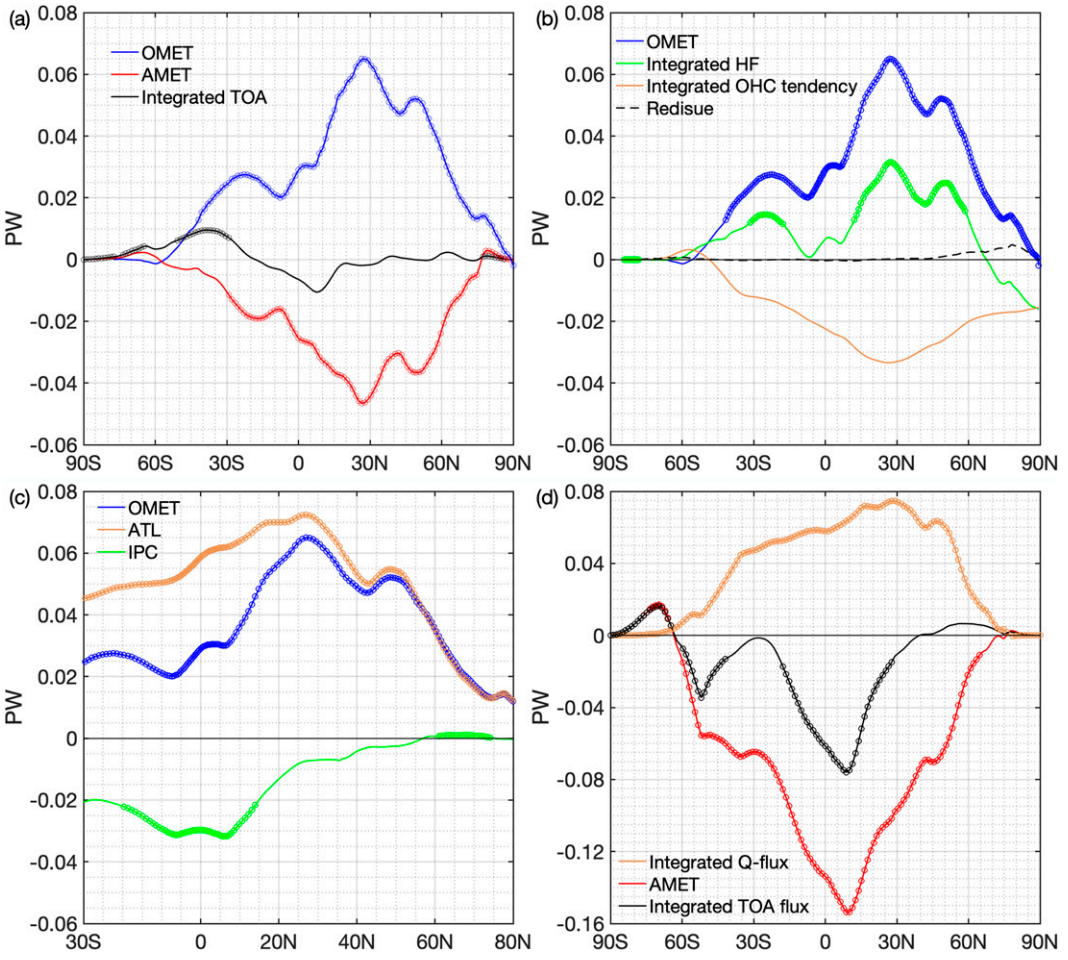

FIG. 5. Anomalous northward energy transports (PW) for (a)–(c) SG minus WK and (d) SG-SOM minus CTL-SOM. Atmospheric transport (AMET; red line) and total oceanic transport (OMET; blue line) are shown in (a). The black line indicates the total energy transport implied by the net radiative flux at the TOA. Quantification of the terms of Eq. (1) is shown in (b). The brown line depicts the effect of ocean heat content (OHC) changes, and the green line shows the heat transport implied by the total heat flux (positive downward). The anomalous OMET [same as (a)] and the residue term are indicated by blue and dashed black lines. The global OMET anomaly [blue, same as (a) and (b)] and its Atlantic (brown) and Indo-Pacific (green) components are shown in (c). Energy transport implied by the anomalous Q flux (brown) in SG-SOM, integrated net radiative flux at TOA (black), and AMET (red) in SG-SOM minus CTL-SOM are shown in (d). Circles indicate a significance level below 5%.

and SOM experiments show an abnormal cross-equatorial Hadley cell in the tropics between 20°S and 20°N. The AMET is mainly due to the geopotential transport in the upper branch of the Hadley cells. The abnormal cross-equatorial Hadley cell therefore transports energy southward. The corresponding heat and moisture transports in the lower branch are oriented northward, consistent with the northward ITCZ shift found previously. However, the response of the Hadley cell is 4 times larger in the SOM simulations (cf. the scales in Figs. 6a and 6b), as is the impact on tropical precipitation.

The wind stress change is illustrated in Figs. 7b and 7c. The zonal mean zonal wind response is also shown in Figs. 8a and 8c. Between 20°S and 20°N, the trade winds decrease in the Northern Hemisphere and increase in the Southern Hemisphere. The changes exhibit a similar pattern in the SOM and AOGCM, but the anomalies are again larger in the SOM experiments. Similar associations among the Hadley cell, precipitation, and trade wind anomalies are found in many other studies (e.g., McGee et al. 2018; Moreno-Chamarro et al. 2019). The tropical wind stress and the associated wind-driven Ekman transport explain the formation of the two STCs around the equator in the tropical ocean in the mean climate. In the Indo-Pacific, the mean STCs are simulated in IPSL-CM6A-LR, as shown with contours in Fig. 7a. In SG minus WK, the anomalous surface northward cross-equatorial Hadley cell results in anomalous southeasterlies in the Southern Hemisphere and southwesterlies in the Northern Hemisphere (Figs. 7b,c). This leads to an anomalous southward Ekman flow on both sides of the equator. The change in the trade winds' direction is located at the equator, which might reflect the change of the Coriolis force sign when crossing the

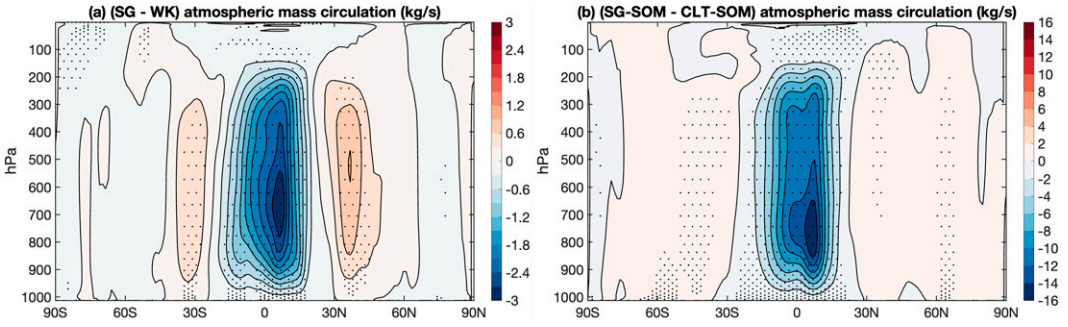

FIG. 6. (a) Mean (black contours) and anomalous (colors) atmospheric overturning mass streamfunction (kg s^{-1}) for SG minus WK. (b) As in (a), but for SG-SOM minus CTL-SOM. The streamfunction is positive for clockwise rotation. Stipples indicate the 5% significance level.

equator. At the equator, the Ekman flow is negligible, but the negative wind stress curl anomaly leads again to a southward flow in the ocean following the Sverdrup balance. The anomalous trade winds, therefore, force a southward flow in the upper ocean. Such southward upper ocean flow is consistent with the abnormal Indo-Pacific oceanic meridional streamfunction (Fig. 7a), which is a counterclockwise cell between 20°S and 25°N. This is also in agreement with the southward OMET anomaly in the Indo-Pacific obtained in Fig. 5c. In the SOM case, the cross-equatorial wind stress anomaly displays a similar structure with a larger amplitude (Fig. 7c). However, the ocean is motionless in SOM. There is thus no compensating southward OMET. The stronger trades in the Southern Hemisphere increase the evaporation, which cools the SST through a wind–evaporation–SST feedback (Xie 1999).

c. *Decomposition of AMET*

To better distinguish the roles of different dynamical processes in the atmosphere, we further decompose the AMET into contributions from transient eddies (TRS) and the sum of mean meridional circulations and stationary waves (MMC + STN):

$$\mathrm{AMET}(\varphi) = \frac{2\pi R_T \cos(\varphi)}{g}\int_{p_s}^{0} \underbrace{[\overline{v}][\overline{\mathrm{MSE}}] + [v'^{*}\overline{\mathrm{MSE}}^{*}]}_{\mathrm{MMC+STN}} + \underbrace{[\overline{v'\mathrm{MSE}'}]}_{\mathrm{TRS}}\, dp, \tag{3}$$

where p_s is the surface pressure, v is the meridional velocity, and g is the gravitational acceleration (Lorenz 1967). An overbar denotes time averages (here, monthly climatologies), and a prime denotes the departure from the time average. Square brackets are zonal averages. The asterisk denotes the departure from the zonal average. MSE denotes the moist static energy, which is computed as the sum of sensible, latent, and potential energy:

$$\mathrm{MSE} = C_{p,a}T_a + Lq + gz, \tag{4}$$

where $C_{p,a}$ is the specific heat of the air at constant pressure, T_a is the air temperature, and L is the latent heat; q is the specific humidity, and z is the geopotential height.

The MSE transports terms are not saved online. Such terms are reconstructed from the monthly outputs. We first compute the mean meridional circulation terms, i.e., the first and second terms on the rhs of Eq. (3), using the monthly climatologies. Then, the TRS component is calculated as the residue of the total AMET calculated previously from the TOA and surface fluxes.

In IPSL-CM6A-LR, as expected, the mean MMC + STN dominates the total transport between 30°S and 30°N, with a maximum of 2.5 PW due to the Hadley cells (Fig. S6). The mean TRS component dominates poleward of 30° in both hemispheres and is associated with the transport by baroclinic eddies and peaks in midlatitudes with an amplitude of 4 (6) PW at 40°N (40°S). The MMC + STN and TRS components are almost identical for the AOGCM and SOM experiments (not shown).

In SG minus WK, the anomalous southward AMET is primarily due to the MMC+STN component in the tropics (Fig. 8b), consistent with a dominant role of the cross-equatorial Hadley cell. The anomalous eddy transport (TRS) dominates in the midlatitudes. In the fully coupled case, the TRS anomaly, like the total southward AMET, is much larger in the Northern Hemisphere. The weakened TRS is related to a reduced meridional temperature gradient in the lower troposphere, and to the reduction of baroclinicity and storm track activity over the North Pacific, North Atlantic, and northern Europe, as shown by the modification of eddy meridional heat flux at 850 hPa (Fig. S7). For SG minus WK, a small reduction of the zonal wind is shown at 40°N in Fig. 8a, which coincides with the weaker storm track activity. Conversely, in the Southern Hemisphere at 30°S and the eddy-driven jet increases. In the SOM case, the AMET and eddy transport changes are more symmetrical around the equator. The Northern Hemisphere changes are similar and larger and are superimposed with an increasing southward AMET in the Southern Hemisphere midlatitudes. This is consistent with the cooling imposed in the Southern Ocean in SG-SOM, which increases the meridional lower tropospheric temperature gradient. Such changes in the Southern Hemisphere are amplified and shifted toward 60°–30°S in the SOM experiments compared to the AOGCM. Last, we note similar zonal mean zonal changes in SG-SOM and SGS-SOM, which suggests that the

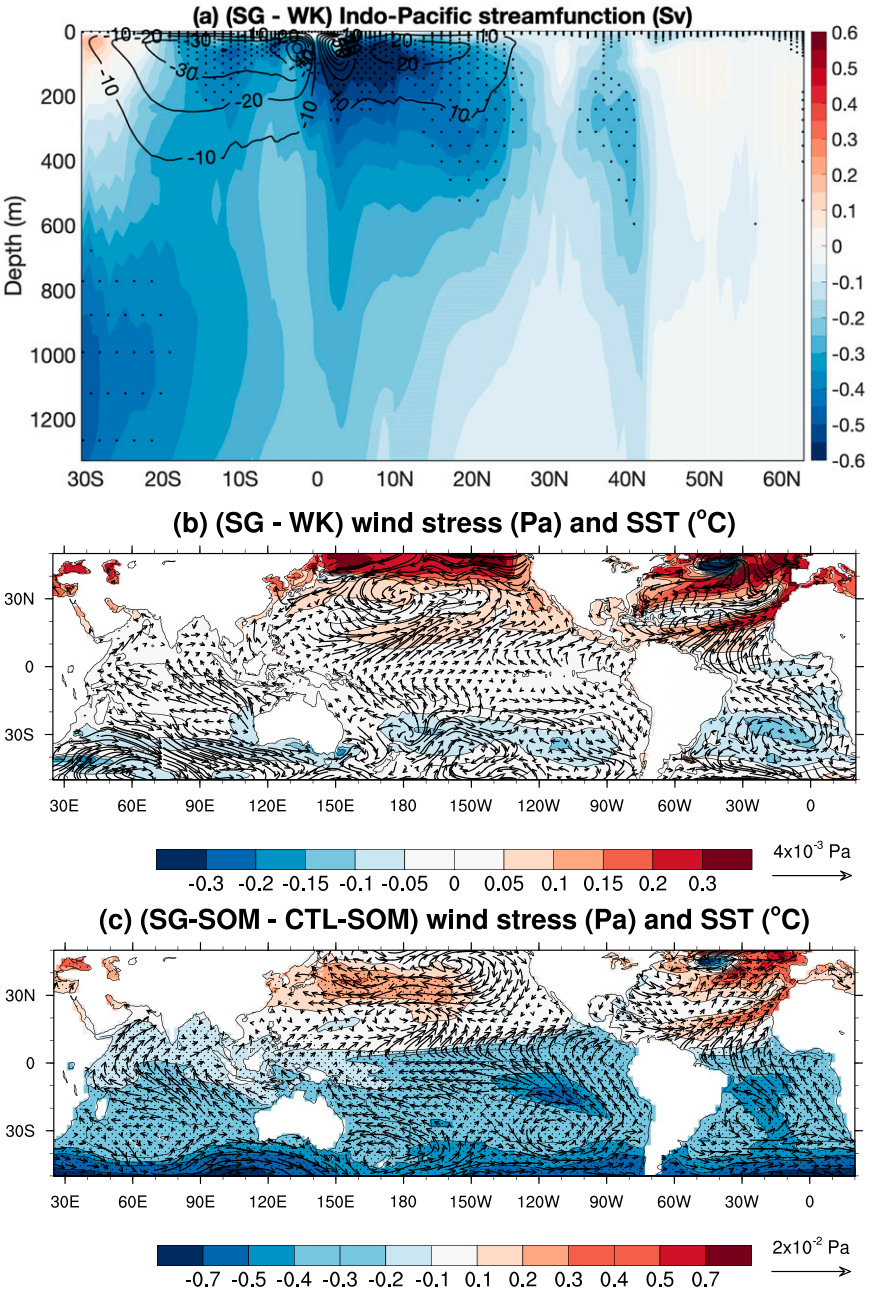

FIG. 7. (a) Anomalous (shading) and mean (contours) Indo-Pacific Ocean overturning streamfunction (Sv) for the AOGCM (SG minus WK). (b) Anomalous wind stress (vectors; Pa) and sea surface temperature (SST; shading; °C) for SG minus WK. (c) As in (b), but for SG-SOM minus CTL-SOM. Stipples indicate a significance level above 95% for SST.

Q-flux pattern does not play an important role in atmospheric circulation changes.

In summary, in the coupled simulations, the imposed Atlantic OMET associated with the AMOC intensification is not fully compensated by a southward AMET. This is because of the increased OHC in the North Atlantic and the decreased OHC south of 30°N, which reduces the "need" for a compensating southward AMET. Then, the OMET is balanced primarily by a southward AMET by eddies in the midlatitudes. In the tropics, the southward AMET is mainly due to the anomalous cross-equatorial Hadley cell. Such Hadley cell response forces an overturning cell in the Indo-Pacific Ocean that transports southward an amount of energy similar to the AMET at the equator.

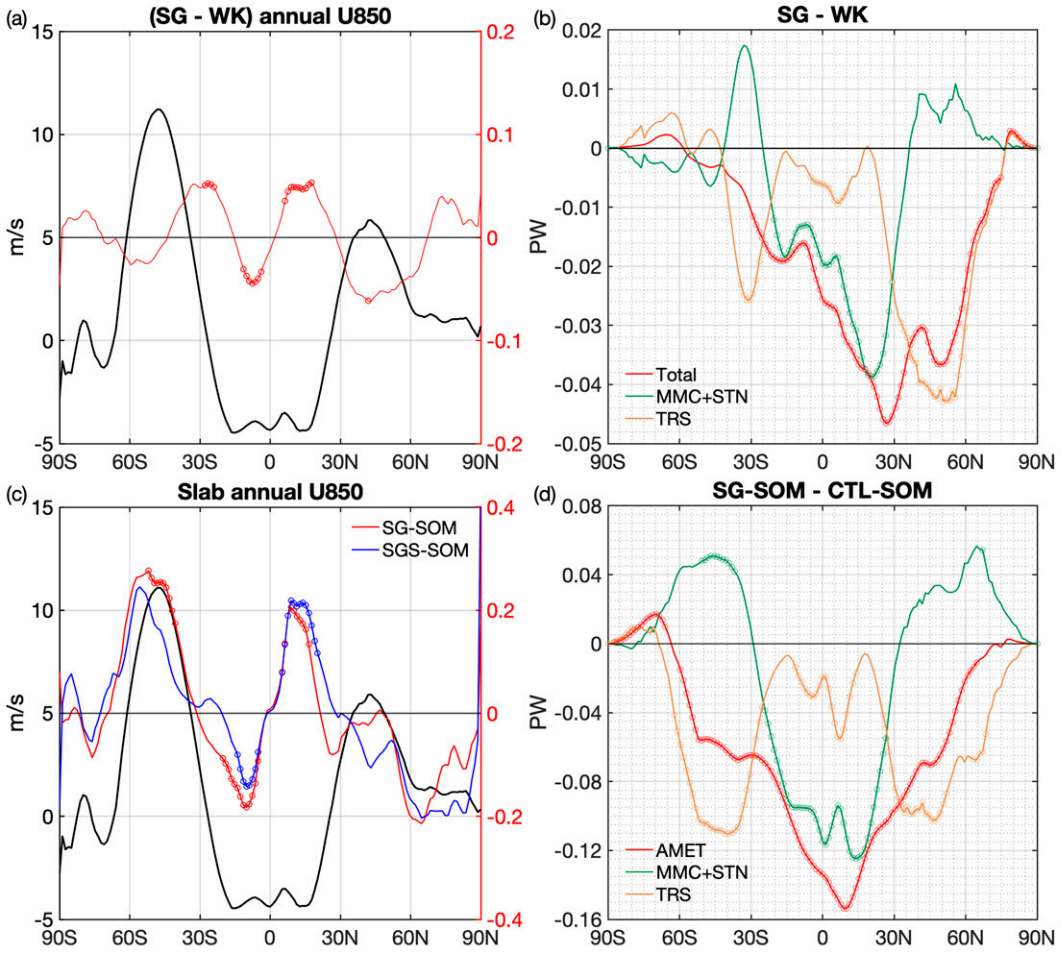

FIG. 8. (a) Mean (black, left y axis) and anomalous (red, right y axis) annual mean, zonal wind at 850 hPa (m s^{-1}) for SG minus WK. (b) Decomposition of the AMET anomaly (red; PW) into the contributions of transient eddies (TRS, brown) and the sum of mean meridional circulation and stationary waves (MMC + STN, green). (c),(d) As in (a) and (b), but for SG-SOM minus CLT-SOM. In (c), SGS-SOM minus CTL-SOM is shown in blue line. Circles indicate the 5% significance level.

The absence of a dynamical ocean in the SOM simulations leads to considerably larger atmospheric responses than in the AOGCM, especially in the tropics (Figs. 3, 6, and 8). First, the global heat content does not change much. Second, the lack of Indo-Pacific Ocean transport means that all of the anomalous transport in the tropics needs to be completed by the atmosphere. Finally, in the SOM simulation, the tropical TOA radiative fluxes vary and lead to an additional southward transport across the equator (Fig. 5d). We thus turn now to these radiative fluxes at the TOA to better understand their variations in the SOM simulations.

5. Radiative feedbacks

The response of the net radiative fluxes at the TOA to a stronger AMOC show similar patterns in the North Atlantic Ocean for the AOGCM and SOM experiments (Figs. 9a,b). In both cases, the largest TOA increase is located at the sea ice edges, in the Labrador and Barents Seas (Figs. 9a,b). As sea ice decreases, the surface albedo decreases, which reduces the reflected shortwave and increases the net TOA radiative fluxes. The fluxes also decrease slightly in the eastern subpolar gyre and Nordic seas, presumably because the warmer temperature there leads to more outgoing infrared radiation.

In the tropics, the responses are again broadly similar, but the amplitude is much larger in the SOM simulations, and the anomalies are more significant: there is a general increase of the incoming radiation in a band around 10°–20°N north of the ITCZ, and a decrease south of the ITCZ and over the eastern tropical ocean basins of the Southern Hemisphere. In the case of SG minus WK, these tropical changes are restricted to the Atlantic and southern Pacific Oceans. To pinpoint the origin of these radiative changes, we illustrate the TOA net radiative flux for clear-sky conditions (Fig. 9c). As the AOGCM and SOM experiments show qualitatively similar changes (not shown), we only illustrate the larger

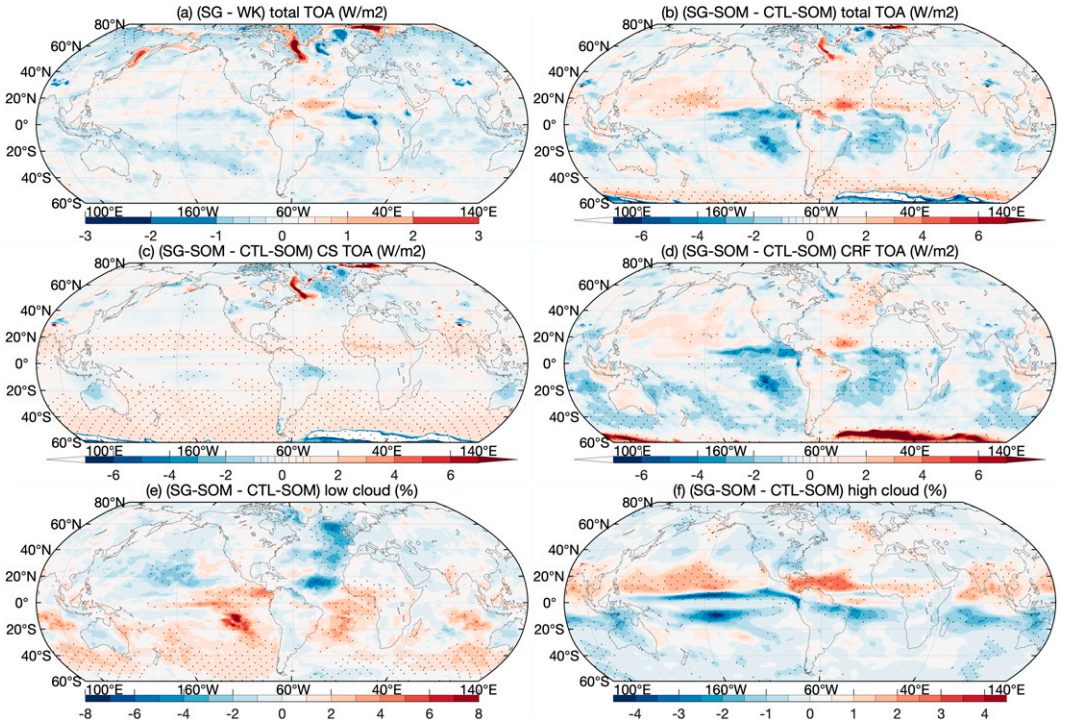

FIG. 9. Anomalous net radiative flux (W m^{-2}) at the top of atmosphere (TOA) for the (a) AOGCM (SG minus WK) and (b) slab-ocean model (SG-SOM minus CTL-SOM). The net radiative flux in the slab-ocean model simulations is decomposed into (c) clear-sky (CS) and (d) cloud radiative forcing (CRF) (W m^{-2}). The flux is positive downward. (e) Low and (f) high cloud anomalies in slab-ocean model (%). Circles indicate the 5% significance level.

anomalies for the SOM experiments. The clear-sky TOA flux shows an increasing downward flux over a band between the equator and 20°N, with local maxima over the continents: the Sahel and western Africa or India. This can be explained by the anomalous Hadley cell bringing more moisture into the Northern Hemisphere, thereby increasing the local greenhouse effect and decreasing the outgoing longwave radiation. Changes in the midlatitudes are consistent with the surface albedo near the sea ice edge, and temperature elsewhere.

The net cloud radiative forcing (CRF; Fig. 9d), defined as the difference between the net flux and the clear-sky flux at TOA, explains most of the changes over the tropical oceans (cf. Fig. 9b and Fig. 9d). Furthermore, the spatial structure of the CRF coincides with changes in the low cloud cover (Fig. 9e). The amount of low clouds increases significantly in the tropical Southern Hemisphere, where it is colder and where the cross-equatorial cell forces stronger subsidence. The larger albedo reflects more solar radiation, increasing the energy deficit in the Southern Hemisphere. The opposite effects occur in the tropical Northern Hemisphere, with warming, decreased subsidence, reduced low clouds, and more incoming energy. In the extratropics, the low cloud changes follow the fluctuations in SST: cloud cover decreases (increases) over the warming (cooling) sea surface. The high clouds vary as the ITCZ moves northward (Fig. 9f), consistent with previous model studies and satellite observations (Brachet et al. 2012; McCoy et al. 2017; Minobe et al. 2008). However, the high clouds have a relatively minor influence on the net cloud radiative forcing, as commonly found due to competition between the albedo effect and the greenhouse effect (Harrison et al. 1990; Zhang et al. 2010).

Therefore, the TOA flux changes associated with AMOC anomalies are induced mainly in the tropics by the low cloud changes, with a contribution from clear-sky outgoing longwave radiation over the continents. The asymmetric changes on both sides of the equator will be balanced by a more intense southward AMET. A stronger cross-equatorial cell thereby reinforces the asymmetric TOA changes. This provides a positive feedback on ITCZ shifts in the SOM simulations, as shown in L'Hévéder et al. (2015). The AOGCM simulations also demonstrate a small asymmetric TOA anomaly (Fig. 5a, black line), but it is weaker in amplitude and only located over the Atlantic Ocean (cf. Fig. 9a and Fig. 9b).

6. Discussion and conclusions

The climate responses to a fluctuation of the AMOC are examined in an AOGCM, IPSL-CM6A-LR, by constraining the baroclinic component of oceanic currents in the North Atlantic. This method is applied to reproduce the AMOC variation characterized by the multidecadal to centennial variability found in a preindustrial simulation. Two simulations are conducted, showing a steady intensification or reduction of the AMOC. The difference between these two simulations shows an AMOC anomaly with an amplitude remaining of ~1 Sv over 100 years.

The simulations using this flow field correction are an alternative to water-hosing simulations. In some hosing experiments, the surface air temperature or SST associated with the weakened AMOC often shows positive anomalies around the Greenland Sea (Stouffer et al. 2006; Zhang and Delworth 2005), especially when reductions in the AMOC intensity are small (Smith and Gregory 2009). In this study, the SST warming associated with an intensified AMOC is concentrated over the subpolar North Atlantic, with an extension toward the subtropical Atlantic and Arctic. Such a pattern is consistent with that found with statistical methods in control simulations (Delworth and Zeng 2012; Mahajan et al. 2011; Jiang et al. 2021).

Some climate responses found in AOGCM to an enhanced AMOC are consistent with previous studies on the weakened AMOC if the possible nonlinearity in strong and weak AMOC phases is neglected. These include a broad warming of the air temperature in the mid- to high-latitude Northern Hemisphere and a southward displacement of the ITCZ over the tropical Atlantic Ocean. The position of the ITCZ in the Indo-Pacific Ocean is unchanged, unlike previous studies (Vellinga and Wood 2002; Zhang and Delworth 2005; Zhang et al. 2010; Jackson et al. 2015). In midlatitudes, the SLP decreases over the North Atlantic, while the midtropospheric geopotential height increases over the polar cap so that the atmospheric circulation changes are mainly baroclinic. The precipitation also slightly increases by 0.15 mm day^{-1} over the North Atlantic. The anomalies are weaker in the Southern Hemisphere. The weakening of the storm track in the Northern Hemisphere is attributed to the reduced meridional temperature gradient in the lower troposphere, as in previous studies (Frankignoul et al. 2013; Gastineau et al. 2013; Ciasto et al. 2016). Such weakening, obtained here as a response to a strong AMOC, is consistent with the role of the ocean dynamics found in the future intensification of the North Atlantic storm track (Chemke et al. 2022). As the AMOC in AOGCM weakens with the increasing greenhouse gas concentrations, the Atlantic oceanic meridional energy transport (OMET) decreases, strengthening the meridional temperature gradient.

The driving mechanisms behind these responses to AMOC variations are investigated with diagnostics of the energy flow in the climate system. In the AOGCM, an anomalous northward OMET in the Atlantic Ocean is induced by the AMOC constrained to the strong state. The ocean heat content (OHC) increases in the North Atlantic and decreases south of 30°N so that the surface heat flux accounts for only about half of the increased northward OMET. The anomalous atmospheric meridional energy transport (AMET) is oriented southward and compensates for the OMET changes through the Bjerknes compensation. In the Northern Hemisphere midlatitudes, this atmospheric transport is accomplished by anomalous southward transient eddy fluxes, which reduce the storm tracks and the eddy-driven jet. In the tropics, the AMET is achieved by the upper branch of an anomalous cross-equatorial Hadley cell, the ascending part of which is located in the Northern Hemisphere. The associated moisture transport in the lower branch shifts the ITCZ northward in the Atlantic Ocean. The anomalous atmospheric Hadley circulation also triggers a cross-equatorial counterclockwise shallow overturning cell in the Indo-Pacific Ocean between 20°S and 20°N through the Ekman response to wind stress anomalies. The resulting southward transport anomaly in the tropical Indo-Pacific Ocean also acts to balance the constrained northward OMET in the Atlantic Ocean.

To investigate the relative roles of the atmospheric transport, the OHC and the Pacific OMET in the climate responses to the Atlantic OMET variations, slab-ocean model (SOM) experiments are performed with a heat flux that leads to an implied energy transport almost identical to the Atlantic OMET in the AOGCM experiments. To avoid any drift, the anomalous downward heat flux used as the Q flux in the Atlantic basin is compensated by an upward flux in the Southern Ocean. The climate responses are similar to those found in the AOGCM. However, the changes in AMET, Hadley cell, and precipitation in the SOM are 4 times larger than those in the AOGCM. We also find a northward shift of the ITCZ in the tropical Pacific in the SOM, in contrast to the AOGCM experiments.

In the AOGCM, the southward transport implied by the reduced OHC south of 30°N lowers the need for actual compensating southward transport, especially in the Southern Hemisphere. The amplitude of the AMET in the AOGCM is around −0.04 PW in the northern tropics. In the SOM, the AMET is doubled to about −0.08 PW due to the lack of ocean storage. In addition, the oceanic overturning cell in the Pacific Ocean transports about the same amount of energy southward as the atmosphere does in the AOGCM. The absence of ocean dynamics and Indo-Pacific heat flux anomalies in the SOM further increases the AMET to about −0.12 PW. Last, the amplified AMET in the SOM leads to an enhanced positive radiative feedback in the tropics: the ITCZ shift toward the warmer Northern Hemisphere reduces the low cloud cover and the planetary albedo, and increases the free tropospheric moisture, which enhances the greenhouse effect, particularly over continents. As a result, the AMET in the SOM eventually has an amplitude of around −0.16 PW in the tropics, leading to the 4 times larger Hadley cell and precipitation changes in the SOM compared to the AOGCM.

Nevertheless, the comparison between the AOGCM and SOM experiments has limitations. The uniform compensating cooling applied in the Southern Ocean in the SOM experiment might play a large role. For instance, it is possible that if some of the compensating cooling were applied in the Pacific and Indian Oceans, this would reduce the interhemispheric contrast of applied fluxes and result in weaker anomalies. We speculate that this compensation has only a minor effect, as the applied fluxes in the Southern Ocean are moderate and compare well with the flux obtained in the AOGCM (not shown). Furthermore, although the atmospheric response to the AMOC has often been found linear (Gastineau and Frankignoul 2012) with an antisymmetric pattern between the responses to positive and negative AMOC anomalies, the response to the North Atlantic SST changes can be nonlinear (Baek et al. 2021). Here, we assess the AMOC impacts with the difference between a strong and a weak run in the AOGCM, while using the difference between analogous strong and neutral AMOC conditions in the SOM. Additional runs with both the AOGCM and SOM would be needed to evaluate whether the

AMOC impacts are nonlinear and whether this could explain the differences between the AOGCM and SOM runs.

The role of the ocean in damping the ITCZ migration has been pointed out in other model studies (Tomas et al. 2016; Green and Marshall 2017; Kang et al. 2018a). We find that the damping effect is attributed to ocean heat storage and oceanic transport in the upper ocean. Although a strengthening AMOC is more frequently tied to increasing storage in the upper ocean (e.g., Cheng et al. 2021; Latif et al. 2019), we find that the OHC decreases in the Southern, Indian, and Pacific Oceans in response to a stronger AMOC. This heat loss exceeds the increasing OHC in the North Atlantic, as found by Pausata et al. (2015) in response to an intensified AMOC induced by high-latitude volcanic eruptions. The oceanic transport in the Indo-Pacific, driven by the anomalous Hadley circulation through trade winds, is consistent with Green and Marshall (2017). Luongo et al. (2022) rather suggested that the response of the shallow subtropical cells in the Indo-Pacific is buoyancy forced instead of wind driven. However, these studies use latitudinally discrete radiative forcing to drive the interhemispheric transport anomaly, whereas here we focus on AMOC anomalies. The role of Ekman transport in muting the ITCZ displacement is relatively limited, consistent with Kang et al. (2018b).

Our results also reveal some robust teleconnection patterns associated with the enhanced AMOC. For instance, at midlatitudes, we find a positive PNA-like geopotential height anomaly over the Gulf of Alaska in both the AOGCM and SOM simulations. These anomalies have a barotropic structure, as expected from the dominant eddy–mean flow interaction at midlatitudes. This is consistent with the results of Zhang and Delworth (2007), who suggested that the weakening of the Aleutian low in response to North Atlantic warming is driven by a weakened eddy heat flux. Many studies suggested the existence of links between the tropical Atlantic Ocean and El Niño–Southern Oscillation (ENSO) in the tropical Pacific Ocean (Rodríguez-Fonseca et al. 2009; Ruprich-Robert et al. 2017; Orihuela-Pinto et al. 2022), which could also explain the AMOC–PNA link found in our simulations. SST associated with AMOC anomalies can lead to anomalous atmospheric convection and changes in the Walker circulation and trade winds over the Pacific Ocean. As the atmosphere and ocean are tightly coupled in the equatorial Pacific, this leads to tropical Pacific SST anomalies and a PNA-like response in the Northern Hemisphere. This connection between intensified AMOC and the PNA is obtained here in the SOM simulation, without a dynamic ocean. This implies that the ocean dynamics play only a minor role in this teleconnection in the IPSL-CM6A-LR model. More work is needed to investigate in detail the responses in the Pacific Ocean to changes in the ocean circulation in the Atlantic.

Last, the slowdown of the AMOC is a robust feature of model projections of global warming. The alleviated warming in the subpolar North Atlantic SST, known as the North Atlantic warming hole, is often attributed to the decline of the AMOC (Liu et al. 2020; Caesar et al. 2018). However, the amplitude of the AMOC decline in the projections is largely uncertain in models (Weijer et al. 2020) with important remote impacts (Bellomo et al. 2021; Jackson et al. 2022; Chemke 2021). The baroclinic flow constraint method presented here is promising to further quantify the role of uncertainty related to the AMOC weakening in the context of a warming climate.

Acknowledgments. We highly appreciate the reviewers' insightful and helpful comments on this manuscript. We acknowledge the support of the MOPGA doctoral program, and the EUR IPSL Climate Graduate School project managed by the ANR under the "Investissements d'avenir" program with the reference ANR-11-IDEX-0004-17-EURE-0006. This work was performed using HPC resources from GENCI-TGCC A0090107403 and A0110107403. GG and WJ were funded by the JPI climate/JPI ocean ROADMAP project (Grant ANR-19-JPOC-003).

Data availability statement. The numerical model simulations upon which this study is based are too large to archive or to transfer. Instead, we provide all the information needed to replicate the simulations. The model code, the namelist settings, the input data, and some key outputs are available at https://doi.org/10.5281/zenodo.7821500.

REFERENCES

Baek, S. H., Y. Kushnir, W. A. Robinson, J. M. Lora, D. E. Lee, and M. Ting, 2021: An atmospheric bridge between the subpolar and tropical Atlantic regions: A perplexing asymmetric teleconnection. *Geophys. Res. Lett.*, **48**, e2021GL096602, https://doi.org/10.1029/2021GL096602.

Bellomo, K., M. Angeloni, S. Corti, and J. von Hardenberg, 2021: Future climate change shaped by inter-model differences in Atlantic meridional overturning circulation response. *Nat. Commun.*, **12**, 3659, https://doi.org/10.1038/s41467-021-24015-w.

Bjerknes, J., 1964: Atlantic air-sea interaction. *Advances in Geophysics*, Vol. 10, Elsevier, 1–82, https://doi.org/10.1016/S0065-2687(08)60005-9.

Boucher, O., and Coauthors, 2020: Presentation and evaluation of the IPSL-CM6A-LR climate model. *J. Adv. Model. Earth Syst.*, **12**, e2019MS002010, https://doi.org/10.1029/2019MS002010.

Brachet, S., F. Codron, Y. Feliks, M. Ghil, H. L. Treut, and E. Simonnet, 2012: Atmospheric circulations induced by a midlatitude SST front: A GCM study. *J. Climate*, **25**, 1847–1853, https://doi.org/10.1175/JCLI-D-11-00329.1.

Brunnabend, S.-E., and H. A. Dijkstra, 2017: Asymmetric response of the Atlantic meridional ocean circulation to freshwater anomalies in a strongly-eddying global ocean model. *Tellus*, **69A**, 1299283, https://doi.org/10.1080/16000870.2017.1299283.

Buckley, M. W., and J. Marshall, 2016: Observations, inferences, and mechanisms of the Atlantic meridional overturning circulation: A review. *Rev. Geophys.*, **54**, 5–63, https://doi.org/10.1002/2015RG000493.

Caesar, L., S. Rahmstorf, A. Robinson, G. Feulner, and V. Saba, 2018: Observed fingerprint of a weakening Atlantic Ocean overturning circulation. *Nature*, **556**, 191–196, https://doi.org/10.1038/s41586-018-0006-5.

——, G. D. McCarthy, D. J. R. Thornalley, N. Cahill, and S. Rahmstorf, 2021: Current Atlantic meridional overturning

circulation weakest in last millennium. *Nat. Geosci.*, **14**, 118–120, https://doi.org/10.1038/s41561-021-00699-z.

Chemke, R., 2021: Future changes in the Hadley circulation: The role of ocean heat transport. *Geophys. Res. Lett.*, **48**, e2020GL091372, https://doi.org/10.1029/2020GL091372.

——, L. Zanna, C. Orbe, L. T. Sentman, and L. M. Polvani, 2022: The future intensification of the North Atlantic winter storm track: The key role of dynamic ocean coupling. *J. Climate*, **35**, 2407–2421, https://doi.org/10.1175/JCLI-D-21-0407.1.

Cheng, L., and Coauthors, 2021: Upper ocean temperatures hit record high in 2020. *Adv. Atmos. Sci.*, **38**, 523–530, https://doi.org/10.1007/s00376-021-0447-x.

Cheng, W., J. C. H. Chiang, and D. Zhang, 2013: Atlantic meridional overturning circulation (AMOC) in CMIP5 models: RCP and historical simulations. *J. Climate*, **26**, 7187–7197, https://doi.org/10.1175/JCLI-D-12-00496.1.

Cheruy, F., and Coauthors, 2020: Improved near-surface continental climate in IPSL-CM6A-LR by combined evolutions of atmospheric and land surface physics. *J. Adv. Model. Earth Syst.*, **12**, e2019MS002005, https://doi.org/10.1029/2019MS002005.

Chiang, J. C. H., and A. R. Friedman, 2012: Extratropical cooling, interhemispheric thermal gradients, and tropical climate change. *Annu. Rev. Earth Planet. Sci.*, **40**, 383–412, https://doi.org/10.1146/annurev-earth-042711-105545.

Ciasto, L. M., C. Li, J. J. Wettstein, and N. G. Kvamstø, 2016: North Atlantic storm-track sensitivity to projected sea surface temperature: Local versus remote influences. *J. Climate*, **29**, 6973–6991, https://doi.org/10.1175/JCLI-D-15-0860.1.

Cunningham, S. A., and Coauthors, 2007: Temporal variability of the Atlantic meridional overturning circulation at 26.5°N. *Science*, **317**, 935–938, https://doi.org/10.1126/science.1141304.

Day, J. J., J. C. Hargreaves, J. D. Annan, and A. Abe-Ouchi, 2012: Sources of multi-decadal variability in Arctic sea ice extent. *Environ. Res. Lett.*, **7**, 034011, https://doi.org/10.1088/1748-9326/7/3/034011.

Delworth, T. L., and F. Zeng, 2012: Multicentennial variability of the Atlantic meridional overturning circulation and its climatic influence in a 4000 year simulation of the GFDL CM2.1 climate model. *Geophys. Res. Lett.*, **39**, L13702, https://doi.org/10.1029/2012GL052107.

Deser, C., R. A. Tomas, and L. Sun, 2015: The role of ocean–atmosphere coupling in the zonal-mean atmospheric response to Arctic sea ice loss. *J. Climate*, **28**, 2168–2186, https://doi.org/10.1175/JCLI-D-14-00325.1.

Drews, A., and R. J. Greatbatch, 2016: Atlantic multidecadal variability in a model with an improved North Atlantic current. *Geophys. Res. Lett.*, **43**, 8199–8206, https://doi.org/10.1002/2016GL069815.

——, and ——, 2017: Evolution of the Atlantic multidecadal variability in a model with an improved North Atlantic current. *J. Climate*, **30**, 5491–5512, https://doi.org/10.1175/JCLI-D-16-0790.1.

——, ——, H. Ding, M. Latif, and W. Park, 2015: The use of a flow field correction technique for alleviating the North Atlantic cold bias with application to the Kiel climate model. *Ocean Dyn.*, **65**, 1079–1093, https://doi.org/10.1007/s10236-015-0853-7.

Frankignoul, C., G. Gastineau, and Y. O. Kwon, 2013: The influence of the AMOC variability on the atmosphere in CCSM3. *J. Climate*, **26**, 9774–9790, https://doi.org/10.1175/JCLI-D-12-00862.1.

Ganachaud, A., and C. Wunsch, 2003: Large-scale ocean heat and freshwater transports during the World Ocean Circulation Experiment. *J. Climate*, **16**, 696–705, https://doi.org/10.1175/1520-0442(2003)016<0696:LSOHAF>2.0.CO;2.

Gastineau, G., and C. Frankignoul, 2012: Cold-season atmospheric response to the natural variability of the Atlantic meridional overturning circulation. *Climate Dyn.*, **39**, 37–57, https://doi.org/10.1007/s00382-011-1109-y.

——, and ——, 2015: Influence of the North Atlantic SST variability on the atmospheric circulation during the twentieth century. *J. Climate*, **28**, 1396–1416, https://doi.org/10.1175/JCLI-D-14-00424.1.

——, F. D'Andrea, and C. Frankignoul, 2013: Atmospheric response to the North Atlantic Ocean variability on seasonal to decadal time scales. *Climate Dyn.*, **40**, 2311–2330, https://doi.org/10.1007/s00382-012-1333-0.

——, B. L'Hévéder, F. Codron, and C. Frankignoul, 2016: Mechanisms determining the winter atmospheric response to the Atlantic overturning circulation. *J. Climate*, **29**, 3767–3785, https://doi.org/10.1175/JCLI-D-15-0326.1.

Green, B., and J. Marshall, 2017: Coupling of trade winds with ocean circulation damps ITCZ shifts. *J. Climate*, **30**, 4395–4411, https://doi.org/10.1175/JCLI-D-16-0818.1.

Harrison, E. F., P. Minnis, B. R. Barkstrom, V. Ramanathan, R. D. Cess, and G. G. Gibson, 1990: Seasonal variation of cloud radiative forcing derived from the Earth Radiation Budget Experiment. *J. Geophys. Res.*, **95**, 18 687–18 703, https://doi.org/10.1029/JD095iD11p18687.

Hobbs, W., M. D. Palmer, and D. Monselesan, 2016: An energy conservation analysis of ocean drift in the CMIP5 global coupled models. *J. Climate*, **29**, 1639–1653, https://doi.org/10.1175/JCLI-D-15-0477.1.

Hodson, D. L. R., R. T. Sutton, C. Cassou, N. Keenlyside, Y. Okumura, and T. Zhou, 2010: Climate impacts of recent multidecadal changes in Atlantic Ocean sea surface temperature: A multimodel comparison. *Climate Dyn.*, **34**, 1041–1058, https://doi.org/10.1007/s00382-009-0571-2.

Hsiao, W.-T., Y.-T. Hwang, Y.-J. Chen, and S. M. Kang, 2022: The role of clouds in shaping tropical Pacific response pattern to extratropical thermal forcing. *Geophys. Res. Lett.*, **49**, e2022GL098023, https://doi.org/10.1029/2022GL098023.

Jackson, L. C., R. Kahana, T. Graham, M. A. Ringer, T. Woollings, J. V. Mecking, and R. A. Wood, 2015: Global and European climate impacts of a slowdown of the AMOC in a high resolution GCM. *Climate Dyn.*, **45**, 3299–3316, https://doi.org/10.1007/s00382-015-2540-2.

——, R. S. Smith, and R. A. Wood, 2017: Ocean and atmosphere feedbacks affecting AMOC hysteresis in a GCM. *Climate Dyn.*, **49**, 173–191, https://doi.org/10.1007/s00382-016-3336-8.

——, A. Biastoch, M. W. Buckley, D. G. Desbruyères, E. Frajka-Williams, B. Moat, and J. Robson, 2022: The evolution of the North Atlantic meridional overturning circulation since 1980. *Nat. Rev. Earth Environ.*, **3**, 241–254, https://doi.org/10.1038/s43017-022-00263-2.

Jiang, W., 2022: Centennial AMOC variability: Mechanism and impacts. Ph.D. thesis, Sorbonne Université, 189 pp.

——, G. Gastineau, and F. Codron, 2021: Multicentennial variability driven by salinity exchanges between the Atlantic and the Arctic Ocean in a coupled climate model. *J. Adv. Model. Earth Syst.*, **13**, e2020MS002366, https://doi.org/10.1029/2020MS002366.

Johns, W. E., and Coauthors, 2011: Continuous, array-based estimates of Atlantic Ocean heat transport at 26.5°N. *J. Climate*, **24**, 2429–2449, https://doi.org/10.1175/2010JCLI3997.1.

Jungclaus, J. H., H. Haak, M. Latif, and U. Mikolajewicz, 2005: Arctic–North Atlantic interactions and multidecadal variability of the meridional overturning circulation. *J. Climate*, **18**, 4013–4031, https://doi.org/10.1175/JCLI3462.1.

Kang, S. M., Y. Shin, and F. Codron, 2018a: The partitioning of poleward energy transport response between the atmosphere and Ekman flux to prescribed surface forcing in a simplified GCM. *Geosci. Lett.*, **5**, 22, https://doi.org/10.1186/s40562-018-0124-9.

——, ——, and S.-P. Xie, 2018b: Extratropical forcing and tropical rainfall distribution: Energetics framework and ocean Ekman advection. *npj Climate Atmos. Sci.*, **1**, 20172, https://doi.org/10.1038/s41612-017-0004-6.

——, and Coauthors, 2019: Extratropical–Tropical Interaction Model Intercomparison Project (ETIN-MIP): Protocol and initial results. *Bull. Amer. Meteor. Soc.*, **100**, 2589–2606, https://doi.org/10.1175/BAMS-D-18-0301.1.

Klinger, B. A., and J. Marotzke, 2000: Meridional heat transport by the subtropical cell. *J. Phys. Oceanogr.*, **30**, 696–705, https://doi.org/10.1175/1520-0485(2000)030<0696:MHTBTS>2.0.CO;2.

Kwon, Y. O., and C. Frankignoul, 2014: Mechanisms of multidecadal Atlantic meridional overturning circulation variability diagnosed in depth versus density space. *J. Climate*, **27**, 9359–9376, https://doi.org/10.1175/JCLI-D-14-00228.1.

Latif, M., T. Park, and W. Park, 2019: Decadal Atlantic meridional overturning circulation slowing events in a climate model. *Climate Dyn.*, **53**, 1111–1124, https://doi.org/10.1007/s00382-019-04772-7.

L'Hévéder, B., F. Codron, and M. Ghil, 2015: Impact of anomalous northward oceanic heat transport on global climate in a slab ocean setting. *J. Climate*, **28**, 2650–2664, https://doi.org/10.1175/JCLI-D-14-00377.1.

Lindzen, R. S., and S. Nigam, 1987: On the role of sea surface temperature gradients in forcing low-level winds and convergence in the tropics. *J. Atmos. Sci.*, **44**, 2418–2436, https://doi.org/10.1175/1520-0469(1987)044<2418:OTROSS>2.0.CO;2.

Liu, W., A. V. Fedorov, S. P. Xie, and S. Hu, 2020: Climate impacts of a weakened Atlantic meridional overturning circulation in a warming climate. *Sci. Adv.*, **6**, eaaz4876, https://doi.org/10.1126/sciadv.aaz4876.

Liu, Z., and Coauthors, 2021: Acceleration of western Arctic sea ice loss linked to the Pacific North American pattern. *Nat. Commun.*, **12**, 1519, https://doi.org/10.1038/s41467-021-21830-z.

Lorenz, E. N., 1967: The nature and theory of the general circulation of the atmosphere. WMO Rep. WMO-218, 188 pp., https://library.wmo.int/doc_num.php?explnum_id=10889.

Luongo, M. T., S.-P. Xie, and I. Eisenman, 2022: Buoyancy forcing dominates the cross-equatorial ocean heat transport response to Northern Hemisphere extratropical cooling. *J. Climate*, **35**, 6671–6690, https://doi.org/10.1175/JCLI-D-21-0950.1.

Mahajan, S., R. Zhang, and T. L. Delworth, 2011: Impact of the Atlantic meridional overturning circulation (AMOC) on Arctic surface air temperature and sea ice variability. *J. Climate*, **24**, 6573–6581, https://doi.org/10.1175/2011JCLI4002.1.

McCarthy, G. D., and Coauthors, 2015: Measuring the Atlantic meridional overturning circulation at 26°N. *Prog. Oceanogr.*, **130**, 91–111, https://doi.org/10.1016/j.pocean.2014.10.006.

McCoy, D. T., R. Eastman, D. L. Hartmann, and R. Wood, 2017: The change in low cloud cover in a warmed climate inferred from AIRS, MODIS, and ERA-Interim. *J. Climate*, **30**, 3609–3620, https://doi.org/10.1175/JCLI-D-15-0734.1.

McGee, D., E. Moreno-Chamarro, B. Green, J. Marshall, E. Galbraith, and L. Bradtmiller, 2018: Hemispherically asymmetric trade wind changes as signatures of past ITCZ shifts. *Quat. Sci. Rev.*, **180**, 214–228, https://doi.org/10.1016/j.quascirev.2017.11.020.

Meccia, V. L., R. Fuentes-Franco, P. Davini, K. Bellomo, F. Fabiano, S. Yang, and J. von Hardenberg, 2023: Internal multicentennial variability of the Atlantic meridional overturning circulation simulated by EC-Earth3. *Climate Dyn.*, **60**, 3695–3712, https://doi.org/10.1007/s00382-022-06534-4.

Menary, M. B., W. Park, K. Lohmann, M. Vellinga, M. D. Palmer, M. Latif, and J. H. Jungclaus, 2012: A multimodel comparison of centennial Atlantic meridional overturning circulation variability. *Climate Dyn.*, **38**, 2377–2388, https://doi.org/10.1007/s00382-011-1172-4.

Mignot, J., A. Ganopolski, and A. Levermann, 2007: Atlantic subsurface temperatures: Response to a shutdown of the overturning circulation and consequences for its recovery. *J. Climate*, **20**, 4884–4898, https://doi.org/10.1175/JCLI4280.1.

——, and Coauthors, 2021: The tuning strategy of IPSL-CM6A-LR. *J. Adv. Model. Earth Syst.*, **13**, e2020MS002340, https://doi.org/10.1029/2020MS002340.

Minobe, S., A. Kuwano-Yoshida, N. Komori, S.-P. Xie, and R. J. Small, 2008: Influence of the Gulf Stream on the troposphere. *Nature*, **452**, 206–209, https://doi.org/10.1038/nature06690.

Montade, V., M. Kageyama, N. Combourieu-Nebout, M.-P. Ledru, E. Michel, G. Siani, and C. Kissel, 2015: Teleconnection between the intertropical convergence zone and southern westerly winds throughout the last deglaciation. *Geology*, **43**, 735–738, https://doi.org/10.1130/G36745.1.

Moore, G. W. K., R. S. Pickart, I. A. Renfrew, and K. Våge, 2014: What causes the location of the air-sea turbulent heat flux maximum over the Labrador Sea? *Geophys. Res. Lett.*, **41**, 3628–3635, https://doi.org/10.1002/2014GL059940.

Moreno-Chamarro, E., J. Marshall, and T. L. Delworth, 2019: Linking ITCZ migrations to the AMOC and North Atlantic/Pacific SST decadal variability. *J. Climate*, **33**, 893–905, https://doi.org/10.1175/JCLI-D-19-0258.1.

Msadek, R., and C. Frankignoul, 2009: Atlantic multidecadal oceanic variability and its influence on the atmosphere in a climate model. *Climate Dyn.*, **33**, 45–62, https://doi.org/10.1007/s00382-008-0452-0.

Muir, L. C., and A. V. Fedorov, 2015: How the AMOC affects ocean temperatures on decadal to centennial timescales: The North Atlantic versus an interhemispheric seesaw. *Climate Dyn.*, **45**, 151–160, https://doi.org/10.1007/s00382-014-2443-7.

——, and ——, 2017: Evidence of the AMOC interdecadal mode related to westward propagation of temperature anomalies in CMIP5 models. *Climate Dyn.*, **48**, 1517–1535, https://doi.org/10.1007/s00382-016-3157-9.

Orihuela-Pinto, B., M. H. England, and A. S. Taschetto, 2022: Interbasin and interhemispheric impacts of a collapsed Atlantic overturning circulation. *Nat. Climate Change*, **12**, 558–565, https://doi.org/10.1038/s41558-022-01380-y.

Pausata, F. S. R., L. Chafik, R. Caballero, and D. S. Battisti, 2015: Impacts of high-latitude volcanic eruptions on ENSO and AMOC. *Proc. Natl. Acad. Sci. USA*, **112**, 13 784–13 788, https://doi.org/10.1073/pnas.1509153112.

Peings, Y., and G. Magnusdottir, 2014: Forcing of the wintertime atmospheric circulation by the multidecadal fluctuations of

the North Atlantic Ocean. *Environ. Res. Lett.*, **9**, 034018, https://doi.org/10.1088/1748-9326/9/3/034018.

Rahmstorf, S., and Coauthors, 2005: Thermohaline circulation hysteresis: A model intercomparison. *Geophys. Res. Lett.*, **32**, L23605, https://doi.org/10.1029/2005GL023655.

Rodríguez-Fonseca, B., I. Polo, J. García-Serrano, T. Losada, E. Mohino, C. R. Mechoso, and F. Kucharski, 2009: Are Atlantic Niños enhancing Pacific ENSO events in recent decades? *Geophys. Res. Lett.*, **36**, L20705, https://doi.org/10.1029/2009GL040048.

Ruprich-Robert, Y., R. Msadek, F. Castruccio, S. Yeager, T. Delworth, and G. Danabasoglu, 2017: Assessing the climate impacts of the observed Atlantic multidecadal variability using the GFDL CM2.1 and NCAR CESM1 global coupled models. *J. Climate*, **30**, 2785–2810, https://doi.org/10.1175/JCLI-D-16-0127.1.

Schneider, T., T. Bischoff, and G. H. Haug, 2014: Migrations and dynamics of the intertropical convergence zone. *Nature*, **513**, 45–53, https://doi.org/10.1038/nature13636.

Screen, J. A., and Coauthors, 2018: Consistency and discrepancy in the atmospheric response to Arctic sea-ice loss across climate models. *Nat. Geosci.*, **11**, 155–163, https://doi.org/10.1038/s41561-018-0059-y.

Smith, R. S., and J. M. Gregory, 2009: A study of the sensitivity of ocean overturning circulation and climate to freshwater input in different regions of the North Atlantic. *Geophys. Res. Lett.*, **36**, L15701, https://doi.org/10.1029/2009GL038607.

Stouffer, R. J., and Coauthors, 2006: Investigating the causes of the response of the thermohaline circulation to past and future climate changes. *J. Climate*, **19**, 1365–1387, https://doi.org/10.1175/JCLI3689.1.

Sutton, R. T., and D. L. R. Hodson, 2005: Atlantic Ocean forcing of North American and European summer climate. *Science*, **309**, 115–118, https://doi.org/10.1126/science.1109496.

——, and ——, 2007: Climate response to basin-scale warming and cooling of the North Atlantic Ocean. *J. Climate*, **20**, 891–907, https://doi.org/10.1175/JCLI4038.1.

Talley, L. D., 2003: Shallow, intermediate, and deep overturning components of the global heat budget. *J. Phys. Oceanogr.*, **33**, 530–560, https://doi.org/10.1175/1520-0485(2003)033<0530:SIADOC>2.0.CO;2.

Thomas, M. D., and A. V. Fedorov, 2019: Mechanisms and impacts of a partial AMOC recovery under enhanced freshwater forcing. *Geophys. Res. Lett.*, **46**, 3308–3316, https://doi.org/10.1029/2018GL080442.

Thornalley, D. J. R., and Coauthors, 2018: Anomalously weak Labrador Sea convection and Atlantic overturning during the past 150 years. *Nature*, **556**, 227–230, https://doi.org/10.1038/s41586-018-0007-4.

Tomas, R. A., C. Deser, and L. Sun, 2016: The role of ocean heat transport in the global climate response to projected Arctic sea ice loss. *J. Climate*, **29**, 6841–6859, https://doi.org/10.1175/JCLI-D-15-0651.1.

Trenberth, K. E., Y. Zhang, J. T. Fasullo, and L. Cheng, 2019: Observation-based estimates of global and basin ocean meridional heat transport time series. *J. Climate*, **32**, 4567–4583, https://doi.org/10.1175/JCLI-D-18-0872.1.

Vellinga, M., and R. A. Wood, 2002: Global climatic impacts of a collapse of the Atlantic thermohaline circulation. *Climatic Change*, **54**, 251–267, https://doi.org/10.1023/A:1016168827653.

——, and P. Wu, 2004: Low-latitude freshwater influence on centennial variability of the Atlantic thermohaline circulation. *J. Climate*, **17**, 4498–4511, https://doi.org/10.1175/3219.1.

Weijer, W., W. Cheng, O. A. Garuba, A. Hu, and B. T. Nadiga, 2020: CMIP6 models predict significant 21st century decline of the Atlantic meridional overturning circulation. *Geophys. Res. Lett.*, **47**, e2019GL086075, https://doi.org/10.1029/2019GL086075.

Xie, S.-P., 1999: A dynamic ocean–atmosphere model of the tropical Atlantic decadal variability. *J. Climate*, **12**, 64–70, https://doi.org/10.1175/1520-0442(1999)012<0064:ADOAMO>2.0.CO;2.

Zhang, R., 2015: Mechanisms for low-frequency variability of summer Arctic sea ice extent. *Proc. Natl. Acad. Sci. USA*, **112**, 4570–4575, https://doi.org/10.1073/pnas.1422296112.

——, 2017: On the persistence and coherence of subpolar sea surface temperature and salinity anomalies associated with the Atlantic multidecadal variability. *Geophys. Res. Lett.*, **44**, 7865–7875, https://doi.org/10.1002/2017GL074342.

——, and T. L. Delworth, 2005: Simulated tropical response to a substantial weakening of the Atlantic thermohaline circulation. *J. Climate*, **18**, 1853–1860, https://doi.org/10.1175/JCLI3460.1.

——, and ——, 2007: Impact of the Atlantic multidecadal oscillation on North Pacific climate variability. *Geophys. Res. Lett.*, **34**, L23708, https://doi.org/10.1029/2007GL031601.

——, and G. K. Vallis, 2007: The role of bottom vortex stretching on the path of the North Atlantic western boundary current and on the northern recirculation gyre. *J. Phys. Oceanogr.*, **37**, 2053–2080, https://doi.org/10.1175/JPO3102.1.

——, S. M. Kang, and I. M. Held, 2010: Sensitivity of climate change induced by the weakening of the Atlantic meridional overturning circulation to cloud feedback. *J. Climate*, **23**, 378–389, https://doi.org/10.1175/2009JCLI3118.1.

——, R. Sutton, G. Danabasoglu, Y. O. Kwon, R. Marsh, S. G. Yeager, D. E. Amrhein, and C. M. Little, 2019: A review of the role of the Atlantic meridional overturning circulation in Atlantic multidecadal variability and associated climate impacts. *Rev. Geophys.*, **57**, 316–375, https://doi.org/10.1029/2019RG000644.